

This is an Open Access document downloaded from ORCA, Cardiff University's institutional repository: <https://orca.cardiff.ac.uk/id/eprint/143385/>

This is the author's version of a work that was submitted to / accepted for publication.

Citation for final published version:

Zhao, Fang, Berndt, Christian, Alves, Tiago M. , Xia, Shaohong, Li, Lin, Mi, Lijun and Fan, Chaoyan 2021. Widespread hydrothermal vents and associated volcanism record prolonged Cenozoic magmatism in the South China Sea. Geological Society of America Bulletin 133 (11-12) , pp. 2645-2660. 10.1130/B35897.1

Publishers page: <https://doi.org/10.1130/B35897.1>

Please note:

Changes made as a result of publishing processes such as copy-editing, formatting and page numbers may not be reflected in this version. For the definitive version of this publication, please refer to the published source. You are advised to consult the publisher's version if you wish to cite this paper.

This version is being made available in accordance with publisher policies. See <http://orca.cf.ac.uk/policies.html> for usage policies. Copyright and moral rights for publications made available in ORCA are retained by the copyright holders.



Widespread hydrothermal vents and associated volcanism record prolonged Cenozoic magmatism in the South China Sea

Fang Zhao^{a,b}, Christian Berndt^c, Tiago M. Alves^d, Shaohong Xia^{a,b,*}, Lin Li^e, Lijun Mi^f, Chaoyan Fan^{a,b}

^a Key Laboratory of Ocean and Marginal Sea Geology, South China Sea Institute of Oceanology, Innovation Academy of South China Sea Ecology and Environmental Engineering, Chinese Academy of Sciences, Guangzhou 510301, China

^b Southern Marine Science and Engineering Guangdong Laboratory (Guangzhou), Guangzhou 511458, China

^c GEOMAR Helmholtz Centre for Ocean Research Kiel, Wischhofstrasse 1-3, 24148 Kiel, Germany

^d 3D Seismic Lab. School of Earth and Ocean Sciences, Cardiff University, Main Building, Park Place, Cardiff, CF10 3AT, United Kingdom

^e Petrochina Hangzhou Research Institute of Geology, Hangzhou, 310023, China

^f CNOOC Zhanjiang Branch of China National Offshore Oil Corporation Limited, Zhanjiang 524057, China

*shxia@scsio.ac.cn (Shaohong Xia)

ABSTRACT

The continental margin of the northern South China Sea is considered to be a magma-poor rifted margin. This work uses new seismic, bathymetric, gravity and magnetic data to reveal how extensively magmatic processes have reshaped the latter continental margin. Widespread hydrothermal vent complexes and magmatic edifices such as volcanoes, igneous sills, lava flows and associated domes, are confirmed in the broader area of the northern South China Sea. Newly identified hydrothermal vents have crater- and mound-shaped surface expressions, and occur chiefly above igneous sills and volcanic edifices. Detailed stratigraphic analyses of volcanoes and hydrothermal vents suggest that magmatic activity took place in discrete phases between the Early Miocene and Quaternary. Importantly, the occurrence of hydrothermal vents close to the present seafloor, when accompanied by shallow igneous sills, suggest that fluid seepage is still active, well after main phases of volcanism previously documented in the literature. After combining geophysical and geochemical data, this study postulates that the extensive post-rift magmatism in the northern South China Sea is linked to the effect of a mantle plume over a long time interval. We propose that prolonged magmatism resulted in contact metamorphism in carbon-rich sediments, producing large amounts of hydrothermal fluid along the northern South China Sea. Similar processes are expected in parts of magma-poor margins in association with CO₂/CH₄ and heat flow release into sea water and underlying strata.

Keywords: South China Sea; post-rift; magmatism; hydrothermal vents; mantle plume.

1. INTRODUCTION

The South China Sea records a multiphase evolution during the Cenozoic, from the onset of continental rifting to its final breakup stage (Briais et al., 1993; Franke, 2013; Li et al., 2014). It has been previously classified as a magma-poor rifted margin due to the relative absence of significant magmatism during continental rifting and breakup (Xu et al., 2012; Franke, 2013). However, several studies have identified intense post-rift volcanism in parts of the South China Sea in both seismic data and dredge samples (Tu et al., 1992; Zou et al., 1993; Hoang and Flower, 1998; Yan et al., 2006; Xu et al., 2012; Wang et al., 2012; Zhao et al., 2016; Zhang et al., 2016; Song et al., 2017; Xia et al., 2018; Gao et al., 2019; Zhao et al., 2020) (Fig. 1). Volcanic activity in the South China Sea occurred chiefly during the Neogene, suggesting the prolongation of magmatism beyond the continental-breakup stages (Fig. 1). In fact, igneous rocks in the South China Sea comprise two main types: (1) extrusive and intrusive complexes of variable extent (and volumes) occurring in different margin segments (Tu et al., 1992; Hoang and Flower, 1998; Yan et al., 2006; Xu et al., 2012; Wang et al., 2012; Yan et al., 2014; Zhao et al., 2014; Zhao et al., 2016; Zhang et al., 2016; Song et al., 2017; Xia et al., 2018; Gao et al., 2019; Zhao et al., 2020); and (2) massive and scattered high-velocity lower crustal bodies in ‘transitional’ crust separating continental and oceanic domains, not present everywhere in the South China Sea (Nissen et al., 1995; Yan et al., 2001; Wang et al., 2006; Wei et al., 2011; Lester et al., 2014; Pichot et al., 2014; Wan et al., 2017; Xia et al., 2018; Fan et al., 2019) (Fig. 1). Tomographic studies have also revealed low-velocity seismic anomalies beneath parts of the northern and western South China Sea, which are linked to elevated sub-surface temperatures in these regions (Lebedev and Nolet, 2003; Zhao, 2004; Huang et al., 2014; Xia et al., 2016; Xia et al., 2018). Evidence from geochemical data shows extensive Late Cenozoic OIB-type basalts in the South China Sea that are consistent with the presence of a mantle plume (Tu et al., 1992; Wang et al., 2012; Xu et al., 2012; Yan et al., 2014; Xia et al., 2016; Zhang et al., 2018; Yang et al., 2019).

Igneous intrusions are known to alter the sediments they intrude into, causing the release of hydrothermal fluids and gases produced in contact metamorphic aureoles (Bell and Butcher 2002; Jamtveit et al., 2004; Svensen et al., 2004; Planke et al., 2005; Svensen et al. 2006; Svensen et al., 2009; Aarnes et al., 2010; Lizarralde et al., 2010; Grove, 2013; Berndt et al., 2016; Iyer et al., 2017). Such alteration processes can lead to the formation of hydrothermal vent complexes by releasing gases and fluids trapped in sedimentary units and to the ocean and potentially the atmosphere (Jamtveit et al. 2004; Svensen et al. 2004; Hansen, 2006; Lizarralde et al., 2010; Berndt et al., 2016; Iyer et al., 2017; Roelofse et al., 2020).

Sediment core data from the northern South China Sea prove that fluid seepage took place several times during the Quaternary (Liang et al., 2017; Yan et al., 2017; Feng et al., 2018). The combination of ^{14}C dating and seafloor observations at the Haima seeps reveal that fluid seepage occurred in multiple episodes since 6.1 ka b.p. (Liang et al., 2017). Fresh and raw authigenic carbonates, plus brecciated and re-cemented breccias recovered from the Dongsha area, suggest recurrent methane seepage and mud volcanism up to the present day (Yan et al., 2017). Geophysical and geological data also reveal widespread pockmarks, cold seeps and mud volcanoes on the seafloor (Sun et al., 2011; Wang et al., 2014; Chen et al., 2015; Liang et al., 2017; Lu et al., 2017; Yan et al., 2017; Feng et al., 2018; Wang et al., 2018) (Fig. 3). It has been suggested, therefore, that large volumes of fluids were released in association with intense volcanism in the northern South China Sea (Wang et al., 2018). Here, we present new geophysical data suggesting that such fluid seepage features could, in fact, be vents generated by sediment mobilization associated with hydrothermal activity, in response to magma intrusion.

The first aim of this work is to provide an inventory of the different styles of magmatism in the northern South China Sea margin. The second aim is to constrain the timing of the various magmatic and hydrothermal events and put them into context of the geodynamic drivers. Hence, this study provides fundamental insights into: (i) the relative timing of formation of igneous features and hydrothermal vents in the study area, (ii) the origin of hydrothermal activity and its relationship to post-rift volcanism in the South China Sea, and (iii) the significance of widespread hydrothermal venting during the Cenozoic evolution stages of the South China Sea.

2. GEOLOGICAL SETTING

The South China Sea records multiphase continental rifting from early Eocene to late Oligocene, which ultimately led to the formation of an oceanic basin from early Oligocene to the early Miocene (32–15 Ma) (Briais et al., 1993; Li et al., 2014; Zhao et al., 2016; Zhao et al., 2020) (Figs. 1-2). Previous studies suggested that seafloor spreading across the South China Sea occurred in two main tectonic pulses. Recently, the timing of seafloor spreading in the South China Sea was revised from 33 Ma to 15 Ma in the Northeast Sub-basin, and from 23.6 Ma to 16 Ma in the Southwest Sub-basin (Li et al., 2014).

As previously described, there is widespread evidence for intraplate basaltic magmatism along the northern South China Sea margin, the Indochina Peninsula and the South China Sea ocean basin, after the end of continental rifting (Tu et al., 1992; Zou et al., 1993; Hoang and Flowers, 1998; Yan et al., 2006; Fyhn et al., 2009; Wang et al., 2012; Xu et al., 2012; Yan et al., 2014; Zhao et al., 2014; Zhao et al., 2016; Xia et al., 2016; Song et al., 2017; Xia et al., 2018; Zhang et al., 2018; Gao et al., 2019; Zhao et al., 2020) (Fig. 1). Onshore magmatism is particularly well represented in the Leiqiong area, South China and Indochina, where almost continuous sub-aerial volcanism occurred throughout the Neogene (Tu et al., 1992; Hoang and Flowers, 1998; Wang et al., 2012; Yan et al., 2006; Yan et al., 2014). In eastern Vietnam, two active volcanoes are reported and considered as the surface expression of long-lived magmatism (Fig. 1).

Offshore the South China Sea, geological and geophysical data provide evidence for intense Cenozoic magmatism, particularly along its northeast and northwest margins (Zou et al., 1993; Hoang and Flowers, 1998; Yan et al., 2006; Fyhn et al., 2009; Wang et al., 2012; Franke, 2013; Zhang et al., 2016; Zhao et al., 2016; Song et al., 2017; Xia et al., 2018; Fan et al., 2019; Gao et al., 2019; Zhao et al., 2020) (Figs. 1-2). Multiple volcanoes and igneous intrusions are identified in the study area and adjacent regions of the South China Sea. Seismic data and volcanic rocks recovered from boreholes and dredges, together with outcrop analogues, suggest the presence of Miocene to Recent volcanism. In addition, regional uplift, fault reactivation, erosion and accelerated depositional rates after the final stages of continental breakup, are attributed to magmatic activity taking place in the region of interest to this study (Lüdmann and Wong, 1999; Carter et al., 2000; Fyhn et al., 2009; Savva et al., 2013; Zhao et al., 2015; Fan et al., 2019).

The northeast South China Sea comprises two uniform units separated by Horizon T_g; widespread, thick Mesozoic strata below Horizon T_g, and sub-parallel Cenozoic strata above (Zhao et al., 2020) (Figs. 4-5). Mesozoic strata, as revealed by Well LF35-1, are Jurassic and Cretaceous in age (Shao et al., 2007), and are predominantly composed of mudstone and sandstone deposited in marine and non-marine environments. Fluvial-lacustrine sandstone, mudstone and shale dominate in Paleogene source intervals, which are overlain by the Lower Miocene carbonate units. In essence, Neogene strata in the northern South China Sea comprise carbonates, marls, sandstones and shales (Fyhn et al., 2009; Fyhn et al., 2013; Zhao et al., 2016; Yan et al., 2017) (Fig. 2). Extensive carbonate

deposition occurred over structural highs of the northern South China Sea from the Early Miocene to the present day (Fyhn et al., 2009; Wu et al., 2009; Fyhn et al., 2013). In addition, a regionally consistent bottom-current system, active from the Late Miocene, has modified the seafloor on the northwest South China Sea together with turbidity currents and local eddies (Sun et al., 2011; Chen et al., 2018).

3. DATA AND METHODS

In this study we use multi-channel (2D) seismic data acquired by the China National Offshore Oil Corporation (CNOOC) and the China National Petroleum Company (CNPC), together with high-quality multibeam bathymetric, gravity and magnetic data (Figs. 3-9). The multi-channel seismic reflection data cover a large area of the northern South China Sea continental margin (Fig. 3a). Multi-channel seismic lines on the northeast South China Sea were acquired by 576-channel streamers with a shot-point spacing of 37.5 m and a common mid-point spacing of 12.5 m (Zhao et al., 2020). Seismic profiles from the northwest South China Sea have a total penetration depth of 8 s two-way time (TWT), with a bin size of 12.5 m (Sun et al., 2011; Lu et al., 2017). Seismic interpretation was completed using Landmark® software and IHS Kingdom® 8.7. Gravity and magnetic data were acquired along the same ship tracks and processed by Liaohe Field PetroChina in 2007, offering additional information about the location and distribution of volcanic bodies.

In this work, igneous features and hydrothermal vents are mapped on intersecting 2D seismic lines following key concepts for the interpretation of volcanic and hydrothermal edifices (Berndt et al., 2000; Jamtveit et al., 2004; Planke et al., 2005; Svensen et al., 2004; Hansen, 2006; Lizarralde et al., 2010; Jackson et al., 2012; Magee et al., 2013; Reynolds et al., 2017). Given the similar morphologies of volcanic and hydrothermal vents, and their similar location within volcanic complexes, we use the criteria proposed by Reynolds et al. (2017) to distinguish them in seismic data. Exploration wells BY2, BY7-1, CK2 and 121-CM-1X, drilled in the study area, penetrated volcanic rocks adjacently to the study area (Shao et al., 2007; Fyhn et al., 2009; Zhao et al., 2016; Zhang et al., 2020). Based on a dominant seismic frequency of 35 Hz in the interval with igneous sills, and an assumed interval velocity of 5500 m/s (Jackson et al., 2012; Magee et al., 2013), we estimate that igneous sills thicker than 39 m are resolved in our seismic data. Due to the lower resolution of seismic data with depth, a large amount of igneous intrusions thinner than 39 m, or deeply buried, may not be clearly imaged (Schofield et al., 2017; Mark et al., 2018).

Multibeam bathymetry data were processed using CaRIS HIPS, and covered an area of approximately 87,000 km², spanning water depths of 100 m to 5000 m (Fig. 3b). These data were merged with SRTM15+ (https://topex.ucsd.edu/WWW_html/srtm15_plus.html). Seafloor features were later correlated with the underlying geology using the available seismic data (Figs. 6-8), combined with sediment core data from the northern South China Sea. Published seismic stratigraphic models from the northern South China Sea margin provide sedimentological information and age controls for the sedimentary, igneous and hydrothermal features identified in seismic data (Shao et al., 2007; Fyhn et al., 2009; Zhao et al., 2016) (Figs. 2, 4-9).

4. RESULTS

4.1. Regional seismic stratigraphy

Five seismic horizons are defined as shown in Figs. 2 and 4-8. Our seismic-stratigraphic interpretation of key horizons shows that the oldest unconformity T_g coincides with the top of the

170 Mesozoic basement and marks the onset of continental rifting in the South China Sea. Two uniform
171 units separated by Horizon T_g are interpreted in the study area; thick Mesozoic strata and slightly
172 deformed, thin Cenozoic strata (Figs. 4-5) (e.g. LF35-1-1; Shao et al., 2007; Yan et al., 2014).
173 Unconformity T₆₀ represents the Base Miocene unconformity and is associated with the onset of
174 continental breakup in the Southwest Sub-basin (Li et al., 2014; Zhao et al., 2016). Horizon T₅₀
175 represents the end of seafloor spreading in the South China Sea. Horizon T₄₀ comprises the end of the
176 Middle Miocene. Horizon T₃₀ represents an upper Miocene-Pliocene regional unconformity (Figs. 2,
177 4-8).

178

179 **4.2. Interpretation of magmatic bodies**

180 Using the newly acquired seismic and multibeam bathymetry data, widespread intrusive and
181 extrusive bodies along the northern South China Sea have been identified and mapped (Figs. 4-9).
182 Multiple volcanoes, volcanic mounds, igneous sills and lava flows are identified in seismic data and
183 show a wide range of morphologies (Figs. 4-9). Seismic interpretation of igneous complexes is based
184 on the large contrast in acoustic impedance between intruding magma and the host-rock. The
185 interpretation is further supported by adjacent published seismic reflection and drilling data (Figs. 2,
186 4-9).

187 The seismic data show large-scale volcanoes (i.e., extrusive volcanic edifices) on a paleo-
188 seafloor. These volcanoes show strong, positive top reflections, chaotic internal facies (Figs. 5-7),
189 and their recognition is supported by gravity and magnetic data, which show positive gravity and
190 magnetic anomalies that correlate with the size and location of the volcanoes (Fig. 6). They often
191 occur close to the continent-ocean boundary (COB) and form NE- or E-striking ridges (Fig. 3).
192 Multibeam bathymetry data show that they are surrounded by moats (Figs. 3 and 6).

193 Strata beneath Horizon T₄₀ are deformed by these volcanoes (Figs. 4-8). A solitary volcano,
194 recognised in Fig. 7a as a conical feature with a topographic high on the modern seafloor, reaches 15
195 km in diameter. Seismic reflections adjacent to the volcanoes below Horizon T₄₀ (10.5 Ma) are often
196 dragged upward and show onlap terminations onto Horizon T₆₀ and T₄₀ (Figs. 4-8). It is worth noting
197 that strata uplift occurs over some of these extrusive edifices, indicating later intrusive events were
198 likely emplaced (Figs. 6 and 8). Well CK2, which penetrated basement rocks, encountered Late
199 Oligocene (~35.5 Ma) to Early Miocene (~19.6 Ma) pyroclastic basalts based on radiocarbon dates
200 (Zhang et al., 2020). Surrounding the volcanoes, sub-parallel stacked strong amplitude anomalies are
201 observed (Figs. 5a and 7). They have abrupt lateral terminations with their upper surfaces
202 conformable with overlying strata; we interpret them as lava flows.

203 Irregular mounded structures are imaged as high-amplitude top reflections and form a rugged
204 seafloor topography (Figs. 5a, 5c, 7d and 7e). The internal reflections of the mounds show moderate-
205 to high-amplitude reflections typical of volcanoclastic material (Jackson, 2012; Magee et al., 2013;
206 Reynolds et al., 2017). Low-amplitude, discontinuous reflections in chimney zones, and velocity pull-
207 ups beneath the mounds, connect to underlying basement. Lava flow units are often observed around
208 these mounds (Figs. 5a). The seismic facies of the mounds are similar to those found in the Pearl
209 River Mouth Basin, offshore Australia, and the northeastern Atlantic, all interpreted as submarine
210 volcanic mounds (Davies et al., 2002; Hansen, 2006; Schofield and Totterdell, 2008; Jackson, 2012;
211 Magee et al., 2013; Zhao et al., 2014; Zhao et al., 2016; Reynolds et al., 2017). Similar volcanic
212 mounds were sampled by exploration wells BY7-1, BY2 and 121-CM-1X (Fyhn et al., 2009; Zhao et
213 al., 2016) confirming they consist of volcanic rocks (Figs. 2 and 3). Wells BY7-1 and BY2, penetrated
214 buried Early Miocene volcanic complexes in the Baiyun Sag, located SW of the northeast South

215 China Sea (Figs. 2 and 3). These volcanic complexes were interpreted as formed in shallow-marine
216 environments, with petrological evidence from borehole sidewall cores revealing basalt lavas and
217 tuffs intercalated with thin-bedded limestone layers (Zhao et al., 2016). Dated through apatite fission
218 track analyses, more than 500 m of basalt with Middle to Lower Miocene ages, were penetrated by
219 well 121-CM-1X. The drilled volcano was interpreted as submarine due to the presence of quench
220 textures in pillow lavas and intercalated limestone intervals (Fyhn et al., 2009).

221 Several discordant, high-amplitude anomalies with abrupt terminations and complex geometries
222 cut through sedimentary intervals in seismic data (Figs. 4-7, 9). They have saucer-shaped, sheet-
223 shaped, stacked or composite geometries. These features are similar to various igneous sills described
224 on Atlantic continental margins and offshore Australia, all formed by the emplacement of magma
225 (e.g. Berndt et al., 2000; Trude et al., 2003; Planke et al., 2005; Jackson et al., 2012; Magee et al.,
226 2013; Schofield et al., 2017). Igneous sills in the study area are parallel to their host strata, in places
227 showing discordant cross-cutting relationships. They are intruded at distinct stratigraphic levels (Figs.
228 4-7, 9). Slight doming of the strata and chimney-like features occur above sills (Figs. 4-7, 9). Some
229 of the sills form a large-scale interconnected transgressive sill complex at depths of approximately
230 2.5 to 3.5 s TWTT (Fig. 4).

231

232 **4.3. Interpretation of hydrothermal vents**

233 Bathymetric and seismic reflection data reveal numerous mound- and crater-like features (Figs.
234 3-9). Seismic reflections at the top of mound-like features have low to moderate amplitude. The
235 internal seismic character of the mounds is dominated by transparent to stratified, low-moderate
236 amplitude reflections, which are distinct from typical volcanic rocks within the volcanic mounds
237 above (Figs. 4, 7, 8b and 9b). Moreover, no associated lava flows are observed around these mound-
238 like features. Crater-like features are irregular V-shaped, U-shaped and W-shaped depressions
239 covered by up to ~500 m of strata, assuming an interval velocity of 1800 m/s (Figs. 5-9). The
240 sedimentary cover becomes slightly thinner towards the upper slope (Figs. 5, 8 and 9).

241 Mound- and crater-like structures are connected to underlying igneous sills and volcanic edifices
242 by prominent chimney-like or pipe-like structures and faults, recognised as vertical regions of
243 disturbed seismic reflections (Figs. 4-9). Similar mound- and crater-like structures are recognised in
244 regions such as the Vøring and Møre Basins in the Northeast Atlantic (Jamtveit et al., 2004; Svensen
245 et al., 2004; Planke et al., 2005), the Karoo Basin in South Africa (Svensen et al., 2006), the Faroe–
246 Shetland Basin, the Tunguska Basin in Siberia (Bell and Butcher 2002; Hansen, 2006; Svensen et al.,
247 2009; Grove, 2013) and the Guaymas Basin (Gulf of California) (Lizarralde et al., 2010; Berndt et al.,
248 2016). Therefore, we interpret the mound- and crater-like structures in the study area as
249 hydrothermal vents linked to igneous sill tips and volcanic edifices by vertical fluid-migration
250 pathways (Figs. 4-9).

251 The vent conduits reveal two main geometries: (1) chimney or pipe-like, and (2) fault-related.
252 The chimney or pipe-like geometry is recognised as a vertical region of disturbed seismic reflections
253 with local ‘pull-up’ or ‘push-down’ effects in seismic data (Figs. 4-9). Many of the mound-like
254 hydrothermal vents are underlain by seismic velocity ‘pull-ups’ associated with sedimentological or
255 diagenetic changes (Figs. 4, 7d, 8b and 9b) (Kilham et al., 2011). In contrast, the seismic reflections
256 beneath crater-like hydrothermal vents often show ‘push-down’ effects, indicating that fluid flow may
257 still be active (Figs. 5-8). The fault-related geometry, with small depressions along the fault plane is
258 interpreted as conduits which channelled fluid and/or gas advection, and controlled the locations of

the vents (Fig. 4-5, 9d). Therefore, “chimney or pipe zones” and faults serve as fluid pathways linking underlying potential igneous intrusions (and volcanic edifices) to hydrothermal vent complexes.

Hydrothermal vents in the northeast South China Sea

The mound-like hydrothermal vents identified in the study area are either isolated or clustered, 0.5-5 km wide and 50-250 m tall (Figs. 4-5, 9a). They occur above zones of disturbed seismic reflections, a character indicating sediment alteration during venting. The mound-type hydrothermal vents were interpreted as mud volcanoes in previous studies, expressed as a wide region of rugged topography on the modern seafloor (Yan et al., 2017). Crater-like hydrothermal vents, several meters to 10 km wide, are identified along the Dongsha area. Most occur above high-angle, closely-spaced faults that extend upward to the modern seafloor and downward to the deep Mesozoic strata (Figs. 4-5, 9a). Hydrothermal vent conduits on the Dongsha High can extend approximately to 4 s TWTT, affecting Mesozoic and Cenozoic strata (Figs. 4-9). It seems that most vent conduits cut through the modern seafloor (Figs. 4-5, 9a). Correlations with the published seismic stratigraphy indicate that the deeper level with hydrothermal vents is earliest Pliocene in age, whereas the shallower level developed near the modern seafloor (Figs. 4-5, 9a).

Scientific cruises held in 2013-2017 discovered multiple active venting sites in the Dongsha area (Yan et al., 2017). An active hydrothermal vent field is shown in Fig. 4. The newly-discovered mounded vents in Fig. 4 rise up to ~250 m above the modern seafloor. In the area where these hydrothermal vents are mapped, chaotic and low-seismic amplitude seismic facies occur downward to at least 3500 ms TWTT and connect with a large-scale interconnected transgressive sill complex. We therefore interpret these facies as the conduits for the ascending hydrothermal fluids. Seafloor images and sampling from the venting fields of the Dongsha region show widely distributed authigenic carbonates, booming chemosynthetic communities, and elevated dissolved methane concentrations in bottom water (Yan et al., 2017). Geochemical data from elevated methane concentrations in bottom waters (up to 4 times higher than the background average), and the presence of fresh authigenic carbonate nodules with living sessile tubeworms and corals at vent sites, indicate ongoing methane seep and mud volcanism. Raw authigenic carbonates, brecciated, and re-concreted breccias also reveal methane seepage and carbonate formation taking place during multiple episodes (Yan et al., 2017).

A typical cold seep environment was also discovered in the northeast South China Sea (Figs. 3a, 5b and 5e). It occurs above a sill complex recognised in seismic data at a depth of ~2000 to 2600 ms TWTT. Seismic images reveal the occurrence of disturbed strata in association with fluid seepage, and intense faults that may serve as fluid pathways above the sill complex (Figs. 5b and 5e). Seafloor sampling from the cold seep site reveal widespread seep-related carbonates (Tong et al., 2013; Wang et al., 2014). The isotopic composition of seep-related carbonates at this site ($\delta^{13}\text{C}$ of -49.2‰ to -12.3‰) indicates thermogenic methane likely derived from Mesozoic strata (Tong et al., 2013; Wang et al., 2014; Yan et al., 2017).

Hydrothermal vents in the northwest South China Sea

Numerous mound- and crater-like hydrothermal vents are also present in the northwest South China Sea (Figs. 6-9). Crater-like hydrothermal vents are up to 8 km in diameter and 220 m in depth (Fig. 4b). Their shapes range from circular, elongated, crescent to complex geometries (Figs. 3b, 6-9) (Sun et al., 2011; Lu et al., 2017; Chen et al., 2018). Elongated and crescent vents suggestively have their long axis oriented by underlying faults, and were modified by bottom currents, turbidity

304 currents and local eddies (Sun et al., 2011; Chen et al., 2018). Mound-like hydrothermal vents are
305 800–2000 m wide and 60–200 m high (Figs. 3, 6-9). These vents are either relatively isolated or
306 clustered to form ‘compound’ structures. Our results show a wide range of sediment deformation
307 beneath the upper part of these vents (Figs. 6-9). For instance, vent Cv5 developed above multiple
308 sill complexes around a prominent volcano, and connects to the underlying basement by zones of
309 velocity pull-up and low amplitude, discontinuous reflections (Fig. 7b). Several mounded
310 hydrothermal vents (Mvg1) developed above the volcanic mounds, are expressed by their distinct
311 seismic facies and architecture (Fig. 7d).

312 The hydrothermal vents identified in the study area occur at various stratigraphic levels since
313 the Middle Miocene (or older strata) truncating the base of crater-like vents or onlapping mounded
314 vents (Figs. 6-9). The most prominent vents are developed at a single surface close to Horizon T₃₀
315 (5.5 Ma). The clustered mounded hydrothermal vents (Mvg1) observed above the volcanic mounds,
316 at the level of Horizon T₃₀, were likely formed at a later time (Fig. 7d). A large-scale crater-shaped
317 hydrothermal vent (Cv9) is mapped above an underlying volcanic edifice (Figs. 3b and 8a). The plan
318 view geometry of this vent is elliptical, ~ 5 km wide and ~ 500 m tall, based on an interval seismic
319 velocity of 1800 m/s. Vent Cv9 occurs at Horizon T₃₀, which is characterised by an unambiguous
320 erosional geometry with underlying reflections truncated against its base (Fig. 8a). The reflections
321 below vent Cv9 comprise a chimney zone with downwarped, chaotic and low-seismic amplitude
322 seismic facies linked to the volcanic edifice at depth (Fig. 8a). The volcanic edifice has ‘chaotic’
323 seismic reflections in its interior, suggesting that magmatic intrusions are present within this feature
324 (Figs. 8a). Strata uplift occurs over the volcanic edifice, indicating later intrusive events. We interpret
325 the chimney facies as a conduit for the ascending hydrothermal fluids. Vent Cv8 is developed above
326 zones of downwarped, disrupted seismic reflections and vertically connected to igneous intrusions at
327 depth (Fig. 8a). The ‘push-down’ effects beneath the two vents indicate that gas may be still present
328 within these ‘pushed-down’ structures.

329 Two active cold seep sites were identified in the northwest South China Sea using the remotely
330 operated vehicle (ROV) “Haima” in 2015 and 2016, and named at the time as the *Haima cold seeps*
331 (Figs. 3a and 8b) (Liang et al., 2017). At depth, an extrusive volcanic edifice is imaged below the
332 *Haima cold seeps* (Fig. 8b). Chaotic seismic facies within the volcanic edifice and strata uplift above
333 the volcanic edifice indicate that later magmatic intrusions occur in the cold seep field. Seismic
334 amplitude dimming below the seafloor reflects active fluid and gas conduits in the *Haima cold seeps*
335 (Fig. 8b). Seafloor images and samples revealed the presence of broadly distributed tubeworm
336 colonies and mussels, shells of clams and large carbonate blocks in the cold seep field (Figs. 8c and
337 8d) (Liang et al., 2017; Guan et al., 2018; Feng et al., 2018). Geochemical data from carbonate blocks
338 and the presence of oil at the cold seeps suggest complex methanogenic and thermogenic processes
339 in the *Haima cold seeps* (Liang et al., 2017; Feng et al., 2018; Guan et al., 2018). Magma from deep
340 sources, below shallower bottom-simulating reflectors (BSRs) and cold seeps near the seafloor, may
341 have supplied heat to dissociate great amounts of gas hydrate (Fig. 8b) (Wang et al., 2018). The
342 radiocarbon dating performed on bivalve shells and seep carbonates revealed that methane seepage,
343 and associated carbonate formation took place during multiple episodes (Liang et al., 2017; Feng et
344 al., 2018).

345

346 5. DISCUSSION

347

5.1. Significance of widespread magmatism and hydrothermal vents in the South China Sea

Our study shows widespread intrusive and extrusive bodies on the continental margin of the northern South China Sea, with magmatic processes triggering the alteration of organic-rich sediments and releasing hydrothermal fluids and gases by hydrothermal vents (Figs. 3-9). Numerous extrusive volcanic edifices, igneous sills, lava flows and volcanic mounds are imaged in seismic data. Cenozoic continental rifting and post-rift tectonics resulted in the development of numerous faults, which are suggested to provide vertical fluid-migration pathways for the transfer of magma and hydrothermal fluids (Zhao et al., 2016; Zhao et al., 2020).

Igneous sills are as young as Pliocene in age and reflect extensive magmatism within organic-rich mudstones, shales and limestones of the Cenozoic and Mesozoic strata (Figs. 4-9). Chimneys and pipes beneath the hydrothermal vents extend downward and coincide with the tips of the underlying igneous intrusions, suggesting these were the most likely origin of the fluids that mobilized the sediments (Figs. 4-9). The emplacement of magmatic intrusions has been previously suggested to result in the contact metamorphism of organic-rich sediments, producing hydrothermal fluids and gases released via hydrothermal vents (Svensen et al., 2004). Fluids and gases generated by thermogenic processes were likely released to the sea water and, ultimately, the atmosphere through chimneys, pipes or fractures, or trapped in the sedimentary rocks (e.g. Svensen et al., 2004; Planke et al., 2005; Svensen et al., 2009; Lizarralde et al., 2010; Berndt et al., 2016; Iyer et al., 2017) (Figs. 4-9).

The close spatial association among fluid seepage occurring on the seafloor, sub-surface fluid flow, and igneous bodies at depth, indicates that hydrothermal activity is one of main drivers of fluid circulation along the northern South China Sea (Figs. 3-9). We argue that part of the mapped hydrothermal vents are still active based on: a) the fluid seepage and active chemosynthetic communities observed during seafloor imaging and sampling surveys (Figs. 4, 5b and 8b); b) the gas-charged sediments and conduits observed in seismic data through the vent structures (Figs. 4-9); c) the occurrence of hydrothermal vents at the seafloor (Figs. 4-9). Our results stress the importance of magmatic systems as features forcing fluid migration towards the seafloor. Hydrothermal vents sitting above faults propagating onto the seafloor were also recognized as important indicators to active faulting (Cuffaro et al., 2019).

Earlier studies have revealed that hydrothermal vent complexes play an important role in controlling subsurface fluid flow pathways during basin subsidence, which host permeable, open fractures and act as a long-lived zone of fluid focusing migration since the main phases of magmatic expulsion (Svensen et al., 2003; Planke et al., 2005; Rateau et al. 2013; Schofield et al. 2017; Roelofse et al., 2020). It is therefore possible that other overpressured fluids such as hydrocarbons, water, and biogenic gas through hydrothermal vent complexes cannot be expelled in the northern South China Sea.

5.2. Timing of magmatic-hydrothermal activity

Due to the lack of borehole data crossing igneous bodies in this study area, the timing of magma emplacement and related hydrothermal venting could only be constrained by seismic-based techniques, which are based on identifying the relationship between igneous-hydrothermal features and stratigraphic units of known age (Trude et al., 2003; Hansen, 2006). Our results confirm that the continental margin of the northern South China Sea was affected by multiple magmatic events during its post-rift stage (Figs. 4-9). Using onlap relationships onto volcanic features, four extrusive episodes can be dated as Early Miocene, Middle Miocene, Late Miocene and Late Miocene-Pliocene in age

(Figs. 5-8). The occurrence of igneous sills within Pliocene strata also suggests a more recent phase of volcanism (Figs. 5-7). Our interpretation that significant volcanism occurred during the Neogene is also supported by radiometric dating of onshore and offshore volcanic rocks along the northern South China Sea (Tu et al., 1992; Zou et al., 1993; Hoang and Flower, 1998; Yan et al., 2006; Wang et al., 2012; Xu et al., 2012; Yan et al., 2014; Zhao et al., 2016; Zhang et al., 2020). Offshore, early Neogene volcanism is equally supported by Pliocene to early Miocene basalts drilled in the Taixinan Basin, Pearl River Mouth Basin, Zhongjiannan Basin, Xisha High and offshore Vietnam (Fig. 1) (Tu et al., 1992; Zou et al., 1993; Yan et al., 2006; Fyhn et al., 2009; Wang et al., 2012; Zhao et al., 2016; Zhang et al., 2020). Rock samples from the Gaojianshi Island (Pyramid Rock) of the Xisha Islands revealed a seamount age of 2.7 Ma, constraining the age of the basaltic magmatism to the late Pliocene (Zou et al., 1993; Gao et al., 2019). Furthermore, volcanic and intrusive rocks have been dated as ~3–23.8 Ma in the South China Sea ocean basin (Fig. 1) (Tu et al., 1992; Yan et al., 2014; Zhao et al., 2016; Xia et al., 2018; Zhang et al., 2016). Onshore, field geological and borehole data in the Leiqiong area, South China and Indochina reveal multiple volcanic eruptions during the Miocene and the Holocene, with a peak in magmatism recorded from late Pliocene to middle Pleistocene (Tu et al., 1992; Zou et al., 1993; Hoang and Flowers, 1998). The close link between onshore and offshore intraplate volcanism in South China also indicates a potential geodynamic link.

Strata onlap onto mounded vents and truncated strata on the base of crater-type vents represent the paleo-surfaces at the time of igneous intrusion (Hansen, 2006). They reveal that the hydrothermal vent complexes linked to underlying volcanism started to develop since the Middle Miocene (Fig. 4-9). Importantly, some large-scale vents truncate against or onlap onto Horizon T₃₀ (5.5 Ma), indicating that intense hydrothermal venting is broadly documented since the Pliocene (Figs. 4-9). The close association between discrete hydrothermal venting and magmatic activity suggests that prolonged volcanism during the Miocene-Pliocene affected sedimentation in the northern South China Sea.

Our age estimates for the observed volcanism and hydrothermal venting in the northern South China Sea lead us to propose that the magmatic bodies in the study area are related to a long-lived period on volcanism during the Neogene. Therefore, prolonged post-rift magmatic activity is suggested as a fundamental control on seafloor and shallow sub-surface geology after continental breakup was initiated in the South China Sea.

423

424 **5.3. Sources of post-rift magma and hydrothermal fluids**

425 Main causes of intraplate upwelling of magma on continental margins include decompression
426 melting of the lithosphere and plume-related activity. Melting induced by mantle decompression is
427 often associated with continental rifting, and is most likely to occur where the crust is highly stretched.
428 Although the crust beneath the northern South China Sea was thinned following continental rifting,
429 the timing and distribution of igneous bodies in the study area suggest that magmatism is not related
430 to mantle decompression melting since ductile extension ceased in the Early Miocene (Li et al., 2014;
431 Savva et al., 2013; Zhao et al., 2020).

432 With the elimination of decompressive melting due to lithospheric extension, it is more likely
433 that the igneous activity in the northern South China Sea was due to long-lived and deep-seated
434 plume-related activity. Geochemical analysis of Miocene to Recent basalt volcanism in the northern
435 South China Sea, the Indochina Peninsula and the South China Sea ocean basin, reveal typical oceanic
436 island basalt (OIB-type) compositions, suggesting the presence of long-lived, deep-seated mantle
437 plumes in the region (Hoang and Flowers, 1998; Xu et al., 2012; Yan et al., 2014; Zhao et al., 2016;

438 Xia et al., 2016; Xia et al., 2018). Geochemical data from the International Ocean Discovery Program
439 (IODP) Expedition 349 in the South China Sea ocean basin also suggest a strong imprint of a mantle
440 plume in ridge magmatism, proving that this mantle plume promoted the opening of the South China
441 Sea (Zhang et al., 2018; Yang et al., 2019). Moreover, scattered lower crustal high-velocity bodies
442 were identified by refraction seismic studies in our study area, probably representing magmatic
443 intrusions in the lower crust (White and McKenzie, 1989; Geoffroy, 2005; Lester et al., 2014; Pichot
444 et al., 2014; Xia et al., 2018; Fan et al., 2019). Low-velocity anomalies extending down to the lower
445 mantle are imaged and suggest the presence of a layered plume beneath the northern and western
446 South China Sea (Fig. 1d) (Lebedev and Nolet, 2003; Zhao, 2004; Huang et al., 2014; Xia et al., 2016;
447 Xia et al., 2018). Importantly, the thermal structure of profile OBS2011 proves that the main
448 component of surface heat flow is mantle-derived (Dong et al., 2018). Heat flow data collected from
449 the northwest South China Sea show high values of 80–100 mW/m², reaching more than 100 mW/m²
450 in places (Dong et al., 2018).

451 Given the evidence above, the occurrence of widespread post-rift magmatism in the study area
452 was most likely generated by a deep-seated mantle plume beneath a thinned crust, following
453 continental breakup in the South China Sea (Xia et al., 2016; Zhang et al., 2018; Yang et al., 2019).
454 The inferred ages for the main magmatic events in this work are not fully coeval with regional tectonic
455 events in the northern South China Sea, but rather with intense magmatism resulting from enhanced
456 melting induced by mantle convection and the presence of a deeper plume (Huisman and Beaumont,
457 2011). The effective duration of plume activity should correspond to a relatively long interval of time,
458 and can explain the distribution and timing of magmatism and hydrothermal seepage in the South
459 China Sea. Thermal weakening of the lithosphere by the hot mantle also promoted regional uplift,
460 fault reactivation, erosion and accelerated depositional rates around the northern South China Sea
461 (Lüdmann and Wong, 1999; Carter et al., 2000; Fyhn et al., 2009; Savva et al., 2013; Zhao et al.,
462 2015; Zhao et al., 2016; Fan et al., 2019).

463

464 6. CONCLUSIONS

465 From an analysis of bathymetric and multi-channel seismic data, the main conclusions of this
466 work are as follows:

467

468 a) Prolonged magmatic-hydrothermal activity, imaged as extensive magmatic bodies and
469 hydrothermal vents, is typical of the post-rift evolution of the northern South China Sea. Numerous
470 volcanoes, igneous sills and lava flows are identified in seismic data. Hydrothermal vents show as
471 crater- and mound- type structures at the paleo-seafloor, and are formed above igneous sills and
472 volcanic edifices.

473 b) The magmatic bodies and hydrothermal vents occur at various stratigraphic levels, suggesting
474 multiple magmatic-hydrothermal pulses during the Miocene and Pliocene. Hydrothermal vents linked
475 to normal faults and underlying chimney or pipe structures, which formed vertical fluid-migration
476 pathways facilitating the transfer of hydrothermal fluids towards the surface.

477 c) We suggest that a long-lived deep-seated mantle plume resulted in voluminous magmatic
478 activities and hydrothermal seepage on the northern South China Sea margin. This will be an
479 important case-study for the better understanding of the prolonged plume-derived magmatic-
480 hydrothermal activity in a magma-poor rifted margin.

By exploring the regional and temporal extent of magmatic and hydrothermal activity in the northern South China Sea, this work provides new sights on deep mantle evolution, carbon fluxes and basin-scale processes on magma-poor continental margins.

ACKNOWLEDGMENTS

This work study was supported by the Youth Innovation Promotion Association CAS, National Natural Science Foundation of China (Nos. 41706054 and U1701641), Key Special Project for Introduced Talents Team of Southern Marine Science and Engineering Guangdong Laboratory (Guangzhou) (GML2019ZD0204, GML2019ZD0104), National Natural Science Foundation of Guangdong Province (2020A1515010497) and Rising Star Foundation of the South China Sea Institute of Oceanology (NHXX2019DZ0201, NHXX2017DZ0101). We thank China National Offshore Oil Company and Petrochina Hangzhou Research Institute of Geology for providing the data and permission to publish this paper. The authors thank the editor Rob Strachan and the reviewers Nick Schofield and Andrea Billi for their helpful reviews.

REFERENCES

- Aarnes, I., Svensen, H., Connolly, J.A.D., and Podladchikov, Y.Y., 2010, How contact metamorphism can trigger global climate changes: modeling gas generation around igneous sills in sedimentary basins: *Geochimica et Cosmochimica Acta*, v. 74, p. 7179–7195.
- Bell, B., and Butcher, H., 2002, On the emplacement of sill complexes: evidence from the Faroe-Shetland Basin. In: Jolley, D.W., Bell, B.R. (Eds.), *The North Atlantic Igneous Province: Stratigraphy, Tectonic, Volcanic and Magmatic Processes*: Geological Society, London, Special Publications, v. 197, p. 307–329.
- Berndt, C., Skogly, O.P., Planke, S., Eldholm, O., and Mjelde, R., 2000, High-velocity breakup-related sills in the Vøring Basin, off Norway: *Journal of Geophysical Research*, v. 105, no. B12, p. 28443–28454.
- Berndt, C., Hensen, C., Mortera-Gutierrez, C., Sarkar, S., Geilert, S., Schmidt, M., Liebetrau, V., Kipfer, R., Scholz, F., Doll, M., Muff, S., Karstens, J., Planke, S., Petersen, S., Böttner, C., Chi, W.-C., Moser, M., Behrendt, R., Fiskal, A., Lever, M., Su, C.-C., Deng, L., Brennwald, M., and Lizarralde, D., 2016, Rifting under steam — How rift magmatism triggers methane venting from sedimentary basins: *Geology*, v. 44, p. 767–770, doi: 10.1130/g38049.1.
- Briais, A., Patriat, P., and Tapponnier, P., 1993, Updated interpretation of magnetic anomalies and seafloor spreading stages in the South China Sea: implications for the Tertiary tectonics of Southeast Asia: *Journal of Geophysical Research*, v. 98, p. 6299–6328.
- Carter, A., Roques, D., and Bristow, C.S., 2000, Denudation history of onshore Central Vietnam: constraints on the Cenozoic evolution of the western margin of the South China Sea: *Tectonophysics*, v. 322, p. 265–277.
- Chen, J., Song, H., Guan, Y., Yang, S., Pinheiro, L.M., Bai, Y., Liu, B., and Geng, M., 2015, Morphologies, classification and genesis of pockmarks, mud volcanoes and associated fluid escape features in the northern Zhongjiannan Basin, South China Sea: *Deep Sea Research Part II*, v. 122, p. 106–117.
- Chen, J., Song, H., Guan, Y., Pinheiro, L.M., and Geng, M., 2018, Geological and oceanographic controls on seabed fluid escape structures in the northern Zhongjiannan Basin, South China Sea: *Journal of Asian Earth Sciences*, v. 168, p. 38–47.
- Cuffaro, M., Billi, A. et al. 2019, The Bortoluzzi mud volcano (Ionian Sea, Italy) and its potential for tracking the seismic cycle of active faults: *Solid Earth*, v. 10, p. 741–763, <https://doi.org/10.5194/se-10-741-2019>.
- Davies, R.J., Bell, B.R., Cartwright, J.A., and Shoulders, S., 2002, Three-dimensional seismic imaging of Palaeocene dike-fed submarine volcanoes from the northeast Atlantic margin: *Geology*, v. 30, p. 223–226.
- Dong, M., Wu, S., Zhang, J., Xu, X., Gao, J., and Song, T., 2018, Lithospheric structure of the Southwest South China Sea: Implications for rifting and extension: *International Geology Review*, v. 62(7-8), p. 924–937, <https://doi.org/10.1080/00206814.2018.1539926>.
- Fan, C., Xia, S., Cao, J., Zhao, F., Sun, J., Wan, K., and Xu, H., 2019, Lateral crustal variation and post-rift magmatism in the northeastern South China Sea determined by wide-angle seismic data: *Marine Geology*, v. 410, p. 70–87.
- Feng, D., Qiu, J.-W., Hu, Y., Peckmann, J., Guan, H., Tong, H., Chen, C., Chen, J., Gong, S., Li, N., and Chen, D., 2018, Cold seep systems in South China Sea: An overview: *Journal of Asian Earth Sciences*, v. 168, p. 3–16.
- Fyhn, M.B.W., Boldreel, L.O., and Nielsen, L.H., 2009, Geological development of the Central and South Vietnamese margin: implications for the establishment of the South China Sea, Indochinese escape tectonics and Cenozoic volcanism: *Tectonophysics*, v. 478, p. 184–214.

526 Fyhn, M.B.W., Boldreel, L.O., Nielsen, L.H., Giang, T.C., Nga, L.H., Hong, N.T.M., Nguyen, N.D., and Abatzis, I., 2013, Carbonate platform growth
527 and demise offshore Central Vietnam: effects of Early Miocene transgression and subsequent onshore uplift: *Journal of Asian Earth Sciences*, v.
528 76, p. 152-168.

529 Franke, D., 2013, Rifting, lithosphere breakup and volcanism: comparison of magma-poor and volcanic rifted margins: *Marine and Petroleum Geology*,
530 v. 43, p. 63–87.

531 Geoffroy, L., 2005, Volcanic passive margins: *Comptes Rendus Geoscience*, v. 337, no. 16, p. 1395–1408.

532 Gao, J., Bangs, N., Wu, S., Cai, G., Han, S., Ma, B., Wang, J., Xie, Y., Huang, W., Dong, D., and Wang, D., 2019, Post - seafloor spreading magmatism
533 and associated magmatic hydrothermal systems in the Xisha uplift region, northwestern South China Sea: *Basin Research*, v. 31, p. 688– 708,
534 <https://doi.org/10.1111/bre.12338>.

535 Guan, H., Birgel, D., Peckmann, J., Liang, Q., Feng, D., Yang, S., Liang, J., Tao, J., Wu, N., and Chen, D., 2018, Lipid biomarker patterns of authigenic
536 carbonates reveal fluid composition and seepage intensity at Haima cold seeps, South China Sea: *Journal of Asian Earth Sciences*, v. 168, p. 163–
537 172.

538 Grove, C., 2013, Submarine hydrothermal vent complexes in the Paleocene of the Faroe–Shetland Basin: insights from three-dimensional seismic and
539 petrographical data: *Geology*, v. 41, p. 71–74.

540 Hansen, D.M., 2006, The morphology of intrusion-related vent structures and their implications for constraining the timing of intrusive events along
541 the NE Atlantic margin: *Journal of the Geological Society*, v. 163, p. 789–800.

542 Hoang, N., and Flowers, M., 1998, Petrogenesis of Cenozoic basalts from Vietnam: implication for origins of a ‘Diffuse Igneous Province’: *Journal of*
543 *Petrology*, v. 39, p. 369-395.

544 Huang, J., 2014, P- and S-wave tomography of the Hainan and surrounding regions: insight into the Hainan plume: *Tectonophysics*, v. 633, p. 176–192.

545 Huismans, R., and Beaumont, C., 2011, Depth-dependent extension, two-stage breakup and cratonic underplating at rifted margins: *Nature*, v. 473, p.
546 74-79.

547 Iyer, K., Schmid, D.W., Planke, S., and Millett, J.M., 2017, Modeling hydrothermal venting in volcanic sedimentary basins: impact on hydrocarbon
548 maturation and paleoclimate: *Earth and Planetary Science Letters*, v. 467, p. 30–42.

549 Jackson, C.A.-L., 2012, Seismic reflection imaging and controls on the preservation of ancient sill-fed magmatic vents: *Journal of the Geological*
550 *Society of London*, v. 169, p. 503–506.

551 Jamtveit, B., Svensen, H., Podladchikov, Y.Y., and Planke, S., 2004, Hydrothermal vent complexes associated with sill intrusions in sedimentary basins.
552 In: Breitkreuz, C., Petford, N. (Eds.), *Physical Geology of High-Level Magmatic Systems*: Geological Soc Publishing House, Bath, p. 233–241.

553 Kilhams, B., McArthur, A., Huuse, M., Ita, E., and Hartley, A., 2011, Enigmatic large-scale furrows of Miocene to Pliocene age from the central North
554 Sea: current-scoured pockmarks? *Geo-Marine Letters*, v. 31, p. 437–449.

555 Lebedev, S., and Nolet, G., 2003, Upper mantle beneath Southeast Asia from S velocity tomography: *Journal of Geophysical Research*, v. 108, 2048.
556 <http://dx.doi.org/10.1029/2000JB000073>.

557 Lester, R., Van Avendonk, H.J.A., McIntosh, K., Lavier, L., Liu, C.S., Wang, T.K., and Wu, F., 2014, Rifting and magmatism in the northeastern South
558 China Sea from wide-angle tomography and seismic reflection imaging: *Journal of Geophysical Research. Solid Earth*, v. 119, p. 2305–2323,
559 <https://doi.org/10.1002/2013JB010639>.

560 Li, C.F., Xu, X., Lin, J., Sun, Z., et al., 2014, Ages and magnetic structures of the South China Sea constrained by the deep tow magnetic surveys and
561 IODP Expedition 349: *Geochemistry, Geophysics, Geosystems*, v. 15, p. 4958–4983.

562 Liang, Q., Hu, Y., Feng, D., Peckmann, J., Chen, L., Yang, S., Liang, J., Tao, J., and Chen, D., 2017, Authigenic carbonates from newly discovered
563 active cold seeps on the northwestern slope of the South China Sea: Constraints on fluid sources, formation environments, and seepage dynamics:
564 *Deep Sea Research Part I*, v. 124, p. 31–41.

565 Lizarralde, D., Soule, S.A., Seewald, J.S., and Proskurowski, G., 2010, Carbon release by off-axis magmatism in a young sedimented spreading centre:
566 *Nature Geoscience*, v. 4, p. 50–54, doi: 10.1038/ngeo1006.

567 Lu, Y., Luan, X., Lyu, F., Wang, B., Yang, Z., Yang, T., and Yao, G., 2017, Seismic evidence and formation mechanism of gas hydrates in the
568 Zhongjiannan Basin, Western margin of the South China Sea: *Marine and Petroleum Geology*, v. 84, p. 274–288.

569 Lüdmann, T., and Wong, H., 1999, Neo-tectonic regime on the passive continental margin of the northern South China Sea: *Tectonophysics*, v. 311, p.
570 113–138.

571 Magee, C., Hunt-Stewart, E., and Jackson, C.A.-L., 2013, Volcano growth mechanism and the role of sub-volcano intrusions: insight from 2D seismic
572 reflection data: *Earth and Planetary Science Letters*, v. 373, p. 41–53.

573 Mark, N.J., Schofield, N., Pugliese, S., Watson, D., Holford, S., Muirhead, D., Brown, R., and Healy, D., 2018, Igneous intrusions in the Faroe Shetland
574 basin and their implications for hydrocarbon exploration; new insights from well and seismic data: *Marine and Petroleum Geology*, v. 92, p. 733–
575 753.

576 Nissen, S.S., Hayes, D.E., Buhl, P., Diebold, J., Yao, B., Zeng, W., and Chen, Y., 1995, Deep penetrating seismic sounding across the northern margin
577 of the South China Sea: *Journal of Geophysical Research. Solid Earth*, v. 100, B11, p. 22407–22433.

578 Pichot, T., Delescluse, M., Chamot-Rooke, N., Pubellier, M., Qiu, Y., Meresse, F., Sun, G., Savva, D., Wong, K.P., Watremez, L., and Auxière, J.-L.,
579 2014, Deep crustal structure of the conjugate margins of the SW South China Sea from wide-angle refraction seismic data: *Marine and Petroleum*
580 *Geology*, v. 58, p. 627–643.

581 Planke, S., Rasmussen, T., Rey, S.S., and Myklebust, R., 2005, Seismic characteristics and distribution of volcanic intrusions and hydrothermal vent
582 complexes in the Vøring and Møre basins. In: Doré, A.G., Vining, B.A. (Eds.), *Petroleum Geology: North-Western Europe and Global*
583 *Perspectives – Proceedings of the 6th Petroleum Geology Conference*: Geological Society, London.

584 Rateau, R., Schofield, N., and Smith, M., 2013, The potential role of igneous intrusions on hydrocarbon migration, West of Shetland: *Petroleum*
585 *Geoscience*, v. 19, no. 3, p. 259–272, doi:10.1144/petgeo2012-035.

586 Reynolds, P., Schofield, N., Brown, R.J., and Holford, S.P., 2017, The architecture of sub-marine monogenetic volcanoes-insights from 3D seismic data:
587 *Basin Research*, v. 30, p. 437–451, <https://doi.org/10.1111/bre.12230>.

588 Roelofse, C., Alves, T.M., and Omosanya, K.O., 2020, Reutilisation of hydrothermal vent complexes for focused fluid flow on continental margins
589 (Modgunn Arch, Norwegian Sea): *Basin Research*, v. 00, p. 1–24, <https://doi.org/10.1111/bre.12507>.

590 Savva, D., Pubellier, M., Franke, D., Chamot-Rooke, N., Meresse, F., Steuer, S., and Auxière, J.L., 2014, Different expressions of rifting on the South
591 China Sea margins: *Marine and Petroleum Geology*, v. 58, p. 579–598.

592 Schofield, A., and Totterdell, J., 2008, Distribution, timing and origin of magmatism in the Bight and Eucla Basins: *Geoscience Australia*, v. 24, p. 1–
593 19.

594 Schofield, N., Holford, S., Millett, J., Brown, D., Jolley, D., Passey, S. R., Muirhead, D., Grove, C., Magee, C., Murray, J., Hole, M., Jackson, C. A.-L.,
595 and Stevenson, C., 2017, Regional magma plumbing and emplacement mechanisms of the Faroe-Shetland Sill Complex: implications for magma
596 transport and petroleum systems within sedimentary basins: *Basin Research*, v. 29(1), p. 41–63.

597 Senger, K., Roy, S., Braathen, A., Buckley, S. J., Bælum, K., Gernigon, L., Mjelde, R., Noormets, R., Ogata, K., Olaussen, S., Planke, S., Ruud, B. O.,
598 and Tverange, J., 2013, Geometries of doleritic intrusions in central Spitsbergen, Svalbard: An integrated study of an onshore-offshore magmatic
599 province with implications for CO2 sequestration: *Norwegian Journal of Geology*, v. 93, p. 143–166.

600 Shao, L., You, H., Hao, H., Wu, G., Qiao, P., and Lei, Y., 2007, Petrology and depositional environments of Mesozoic strata in the northeastern South
601 China Sea: *Geological Review*, v. 53 (2), p. 164–169, <https://doi.org/10.16509/j.georeview.2007.02.004>.

602 Svensen, H., Jamtveit, B., Planke, S., and Pedersen, T., 2003, Seep carbonate formation controlled by hydrothermal vent complexes: a case study from
603 the Vøring volcanic basin, the Norwegian Sea: *Geo-Marine Letters*, v. 23, p. 351–358.

604 Svensen, H., Planke, S., Malthé-Sorensen, A., Jamtveit, B., Myklebust, R., Rasmussen Eidem, T., and Rey, S.S., 2004, Release of methane from a
605 volcanic basin as a mechanism for initial Eocene global warming: *Nature*, v. 429, p. 542–545.

606 Svensen, H., Jamtveit, B., Planke, S., and Chevallier, L., 2006, Structure and evolution of hydrothermal vent complexes in the Karoo Basin, South
607 Africa: *Journal of the Geological Society*, v. 163, p. 671–682.

608 Svensen, H., Planke, S., Polozov, A.G., Schmidbauer, N., Corfu, F., Podladchikov, Y.Y., and Jamtveit, B., 2009, Siberian gas venting and the end-
609 Permian environmental crisis: *Earth and Planetary Science Letters*, v. 277, p. 490–500.

610 Song, X., Li, C., Yao, Y., and Shi, H., 2017, Magmatism in the evolution of the South China Sea: geophysical characterization: *Marine Geology*, v. 394,
611 p. 4–15, <https://doi.org/10.1016/j.margeo.2017.07.021>.

612 Sun, Q.L., Wu, S.G., Hovland, M., Luo, P., Lu, Y.T., and Qu, T.L., 2011, The morphologies and genesis of mega-pockmarks near the Xisha Uplift, South
613 China Sea: *Marine and Petroleum Geology*, v. 28, p. 1146–1156.

614 Tong, H., Feng, D., Cheng, H., Yang, S., Wang, H., Min, A.G., Edwards, R.L., Chen, Z., and Chen, D., 2013, Authigenic carbonates from seeps on the
615 northern continental slope of the South China Sea: New insights into fluid sources and geochronology: *Marine and Petroleum Geology*, v. 43, p.

260–271.

Trude, K.J., Cartwright, J.A., Davies, R.J., and Smallwood, J.R., 2003, A new technique for dating igneous sills. *Geology*, v. 31, p. 813–816.

Tu, K., Flower, M., Carlson, R., Xie, G., Chen, C., and Zhang, M., 1992, Magmatism in the South China Basin 1. Isotopic and trace-element evidence for an endogenous Dupal mantle component: *Chemical Geology*, v. 97, p. 47–63.

Wan, K., Xia, S., Cao, J., Sun, J., and Xu, H., 2017, Deep seismic structure of the northeastern South China Sea: origin of a high-velocity layer in the lower crust: *Journal of Geophysical Research. Solid Earth*, v. 122 (4), p. 2831–2858, <https://doi.org/10.1002/2016JB013481>.

Wang, T.K., Chen, M., Lee, C., and Xia, K., 2006, Seismic imaging of the transitional crust across the northeastern margin of the South China Sea: *Tectonophysics*, v. 412, p. 237–254.

Wang, K.-L., Lo, Y.-M., Chung, S.-L., Lo, C.-H., Hsu, H.K., Yang, H.-J., and Shinjo, R., 2012, Age and geochemical features of dredged basalts from offshore SW Taiwan: the coincidence of intra-plate magmatism with the spreading South China Sea: *Terrestrial, Atmospheric and Oceanic Sciences*, v. 23, no.6, p. 657–669.

Wang, S., Yan, W., Chen, Z., Zhang, N., and Chen, H., 2014, Rare earth elements in cold seep carbonates from the southwestern Dongsha area, northern South China Sea: *Marine and Petroleum Geology*, v. 57, p. 482–493.

Wang, J., Wu, S., Kong, X., Ma, B., Li, W., Wang, D., Gao, J., and Chen, W., 2018, Subsurface fluid flow at an active cold seep area in the Qiongdongnan Basin, northern South China Sea: *Journal of Asian Earth Sciences*, v. 168, p. 17–26.

Wei, X.D., Ruan, A.G., Zhao, M.H., Qiu, X.L., Li, J.B., Zhu, J.J., Wu, Z.L., and Ding, W.W., 2011, A wide-angle OBS profile across Dongsha Uplift and Chaoshan Depression in the mid-northern South China Sea: *Chinese Journal of Geophysics*, v. 54 (6), p. 1149–1160.

White, R., and McKenzie, D., 1989, Magmatism at rift zone: the generation of volcanic continental margins and flood basalts: *Journal of Geophysical Research*, v. 94, p. 7685–7729.

Wu, S., Yuan, S., Zhang, G., Ma, Y., Mi, L., and Xu, N., 2009, Seismic characteristics of a reef carbonate reservoir and implications for hydrocarbon exploration in deep water of the Qiongdongnan Basin, Northern South China Sea: *Marine and Petroleum Geology*, v. 36, p. 817–823.

Xia, S., Zhao, D., Sun, J., and Huang, H., 2016, Teleseismic imaging of the mantle beneath southernmost China: new insights into the Hainan plume: *Gondwana Research*, v. 36, p. 33–43.

Xia, S., Zhao, F., Zhao, D., Fan, C., Wu, S., Mi, L., Sun, J., Cao, J., and Wan, K., 2018, Crustal plumbing system of post-rift magmatism in the northern margin of South China Sea: New insights from integrated seismology: *Tectonophysics*, v. 744, p. 227–238.

Xu, Y., Wei, J., Qiu, H., Zhang, H., and Huang, X., 2012, Opening and evolution of the South China Sea constrained by studies on volcanic rocks: preliminary results and a research design: *Chinese Science Bulletin*, v. 57, p. 3150–3164.

Yan, P., Zhou, D., and Liu, Z., 2001, A crustal structure profile across the northern continental margin of the South China Sea: *Tectonophysics*, v. 338, p. 1–21, [https://doi.org/10.1016/S0040-1951\(01\)00062-2](https://doi.org/10.1016/S0040-1951(01)00062-2)

Yan, P., Deng, H., Liu, H., Zhang, Z., and Jiang, Y., 2006, The temporal and spatial distribution of volcanism in the South China Sea region: *Journal of Asian Earth Sciences*, v. 27, p. 647–659.

Yan, Q., Shi, X., and Castillo, P., 2014, The late Mesozoic-Cenozoic tectonic evolution of the South China Sea: a petrologic perspective: *Journal of Asian Earth Sciences*, v. 85, p. 178–201.

Yan, P., Wang, Y., Liu, J., Zhong, G., and Liu, X., 2017, Discovery of the southwest Dongsha Island mud volcanoes amid the northern margin of the South China Sea: *Marine and Petroleum Geology*, v. 88, p. 858–870.

Yang, F., Huang, X. L., Xu, Y. G., and He, P. L., 2019, Plume-ridge interaction in the South China Sea: Thermometric evidence from Hole U1431E of IODP Expedition 349: *Lithos*, v. 324, p. 466–478.

Zhang, Q., Wu, S. G., and Dong, D. D., 2016, Cenozoic magmatism in the northern continental margin of the South China Sea: Evidence from seismic profiles: *Marine Geophysical Research*, v. 37, no. 2, p. 71–94.

Zhang, G.L., Luo, Q., Zhao, J., Jackson, M.G., Guo, L.S., and Zhong, L.F., 2018, Geochemical nature of sub-ridge mantle and opening dynamics of the South China Sea: *Earth and Planetary Science Letters*, v. 489, p. 145–155.

Zhang, Y., Yu, K.Y., Qian, H.D., Fan, T.L., Yue, Y.F., Wang, R., Jang, W., Xu, S.D., and Wang, Y.H., 2020, The basement and volcanic activities of the Xisha Islands: Evidence from the kilometer-scale drilling in the northwestern South China Sea: *Geological Journal*, v. 55, p. 571–583.

Zhao, D., 2004, Global tomographic images of mantle plumes and subducting slabs: insight into deep earth dynamics: *Physics of the Earth and Planetary Interiors*, v. 146, p. 3–34.

661 Zhao, F., Wu, S.G., Sun, Q.L., Huuse, M., Li, W., and Wang, Z.J., 2014, Submarine volcanic mounds in the Pearl River Mouth Basin, northern South
662 China Sea: *Marine Geology*, v. 355, p. 162–172.

663 Zhao, F., Alves, T.M., Li, W., and Wu, S., 2015, Recurrent slope failure enhancing source rock burial depth and seal unit competence in the Pearl River
664 Mouth Basin, offshore South China Sea: *Tectonophysics*, v. 643, p. 1–7.

665 Zhao, F., Alves, T.M., Wu, S.G., Li, W., Huuse, M., Mi, L.J., Sun, Q.L., and Ma, B.J., 2016, Prolonged post-rift magmatism on highly extended crust
666 of divergent continental margins (Baiyun Sag, South China Sea): *Earth and Planetary Science Letters*, v. 445, p. 79–91.

667 Zhao, F., Alves, T.M., Xia, S., Li, W., Wang, L., Mi, L., Wu, S., Cao, J., and Fan, C. 2020, Along-strike segmentation of the South China Sea margin
668 imposed by inherited pre-rift basement structures: *Earth and Planetary Science Letters*, v. 530, 115862.

669 Zou, H. P., 1993, On the problem about the crust's, attribution of South China Sea basin - discussion from comparative study on basalts of seamounts
670 in South China Sea basin and the neighboring areas: *Geotectonica et Metallogenia*, v. 17, no. 4, p. 293–303 (in Chinese with English abstract).

FIGURES

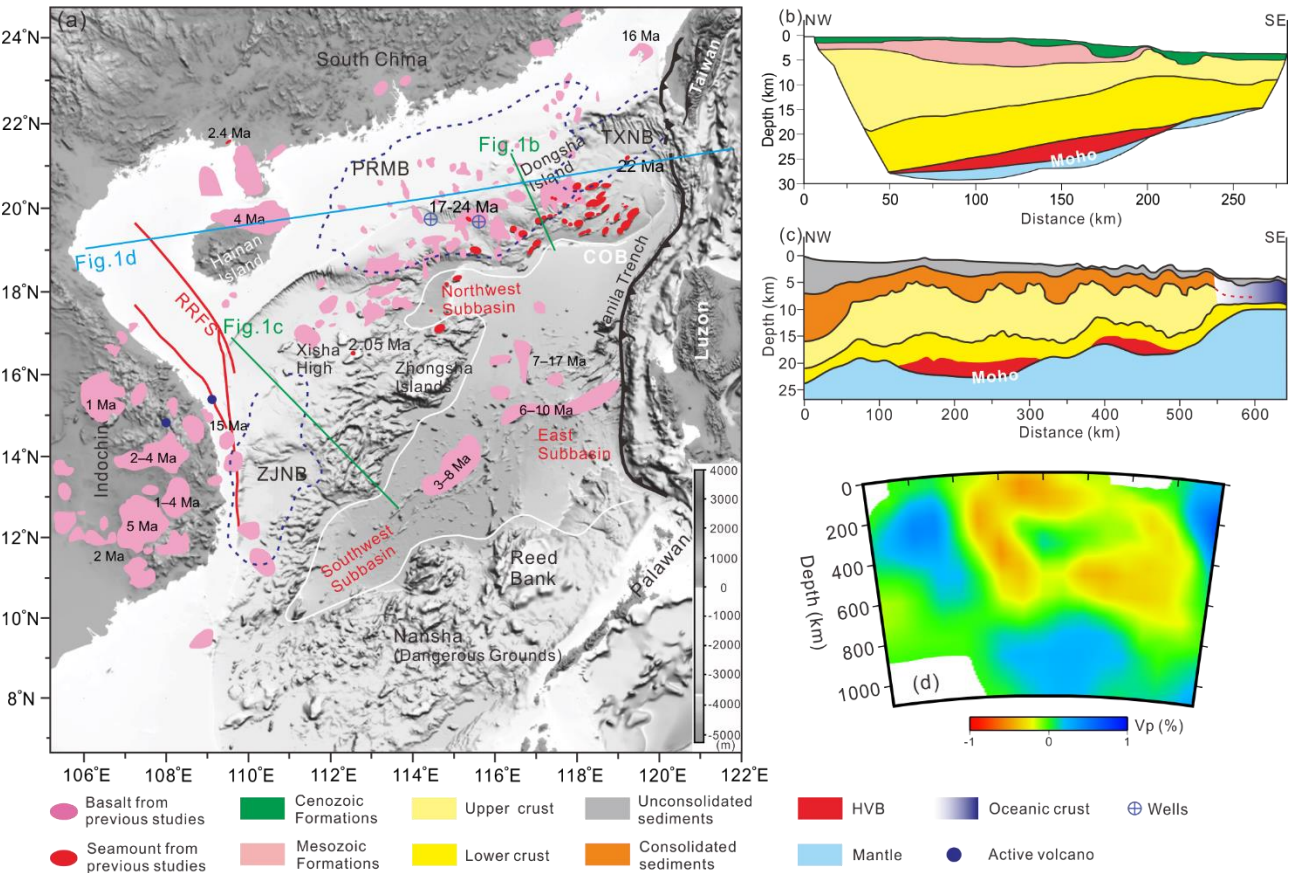


Fig. 1. (a) Regional map of the South China Sea revealing the distribution of the Late Cenozoic volcanism documented in previous work (Tu et al., 1992; Hoang and Flower, 1998; Wang et al., 2012; Yan et al., 2014; Zhao et al., 2016; Xia et al., 2018). Main geomorphological features are labelled. Green lines mark the locations of Figs. 1b and 1c. The blue line marks the location of Fig. 1d. (b) and (c) Velocity profiles crossing the northern South China Sea (see location in Fig.1a) showing the crustal structure of the northern South China Sea as derived from wide-angle seismic data, and the presence of high-velocity bodies (HVBs) in the lower crust (after Pichot et al., 2014 and Fan et al., 2019). (d) Cross-section showing the P-wave velocity structure beneath the northern South China Sea. Large-scale low-velocity anomalies occur towards the Hainan Island and the northeast South China Sea (after Xia et al., 2016). See location of the cross-section in Fig. 1a. TXNB, Taixinan Basin; PRMB, Pearl River Mouth Basin; ZJNB, Zhongjiannan Basin; COB, continent–ocean boundary; RRFS - Red River Fault System; HVB - high-velocity body.

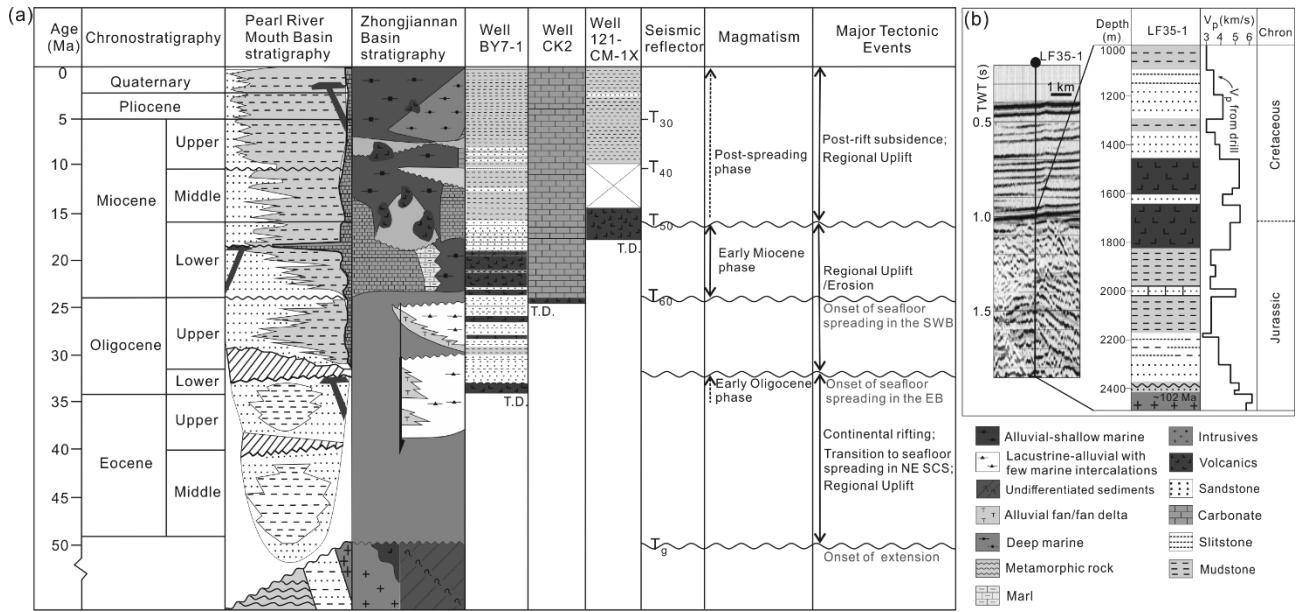


Fig. 2. (a) Summary chart of the northern South China Sea stratigraphy shown together with main tectonic and magmatic events affecting the region (modified after Fyhn et al., 2009, Zhao et al., 2016 and Zhang et al., 2020). (b) Lithologies penetrated by well LF35-1 revealing the depositional setting of Mesozoic strata in the northeast South China Sea (modified after Shao et al., 2007).

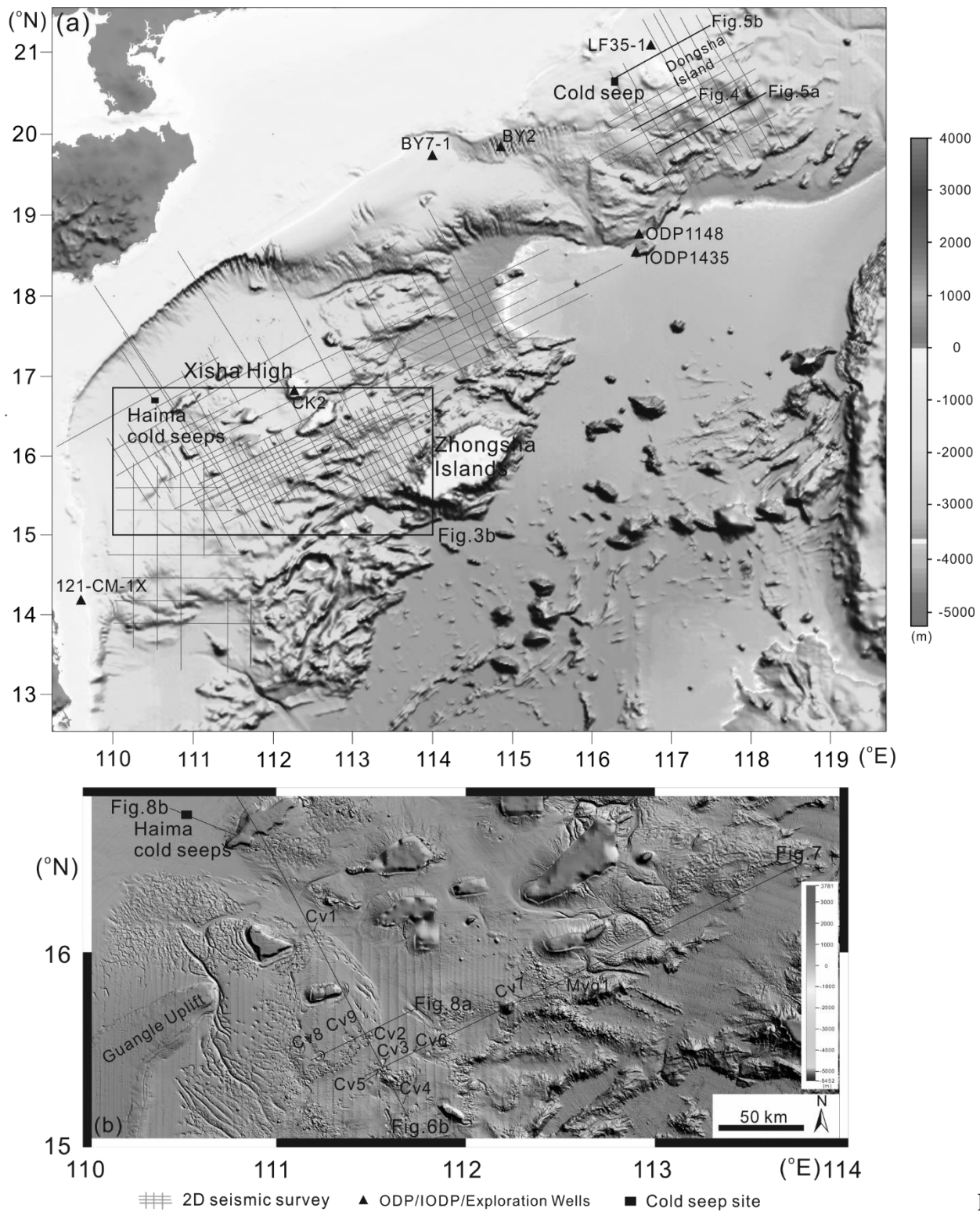


Fig.

3. (a) Structural map showing the locations of multichannel seismic reflection profiles used in this work. The locations of exploration wells, IODP/ODP sites and cold seep sites are shown. The black box marks the location of Fig. 3b. (b) Bathymetric map showing widespread hydrothermal vents in the northwest South China Sea. Black solid lines mark the locations of seismic lines discussed in this work. Fig. 8b is a published seismic profile modified from Wang et al. (2018). The locations of figures, the *Haima cold seeps* and hydrothermal vents identified from multi-channel seismic profiles are labelled in the figure.

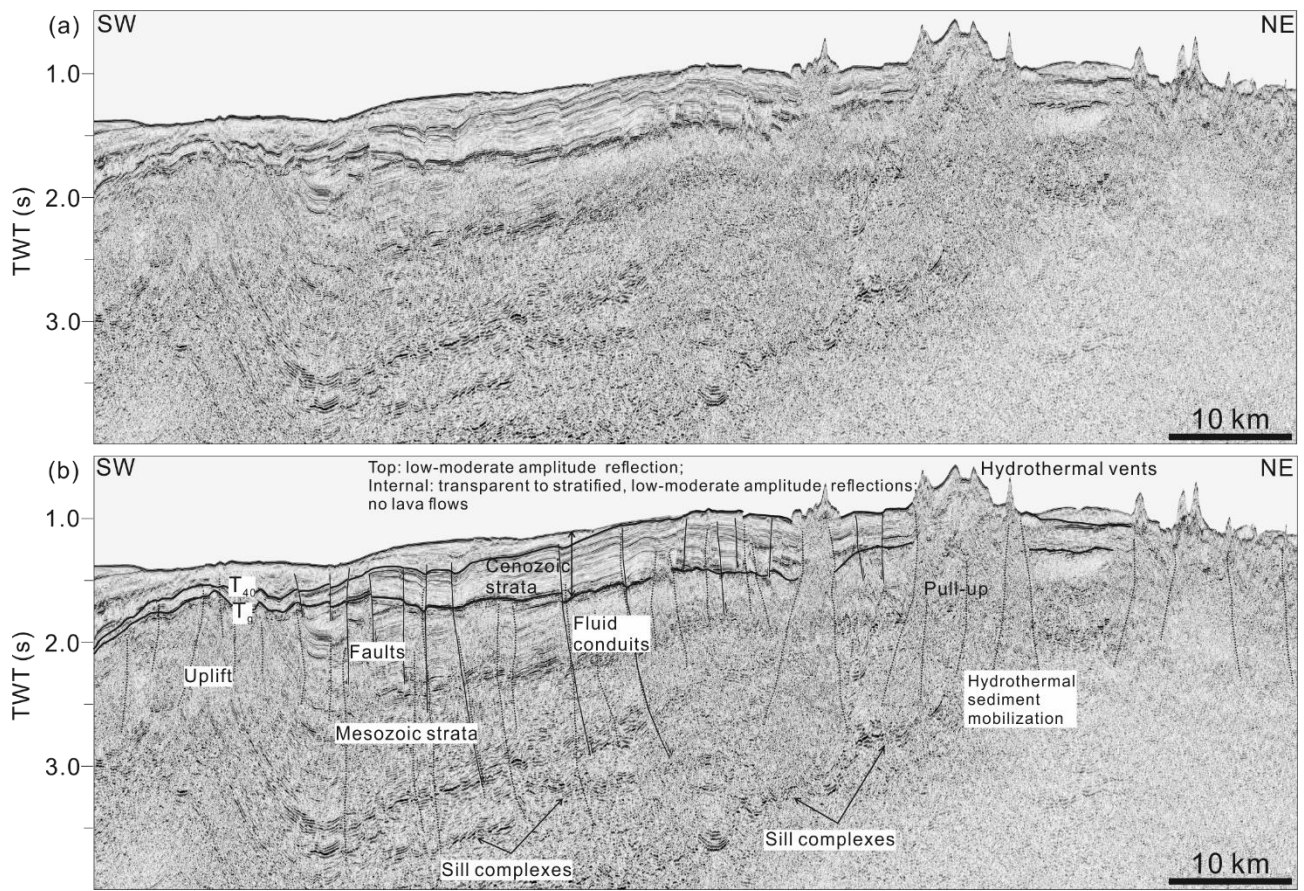


Fig. 4. (a) and (b) Uninterpreted and interpreted multichannel seismic profile (see location in Fig. 3a) across the northeast South China Sea showing key seismic horizons and mound-shaped hydrothermal vents. Horizons T₄₀ and T_g correspond to the base of upper Miocene strata and the top of basement, respectively. Numerous sills and sill complexes are identified in Mesozoic strata. Note that mounded vents occur above deep igneous sill complexes and are linked to these latter by prominent chimney-like structures.

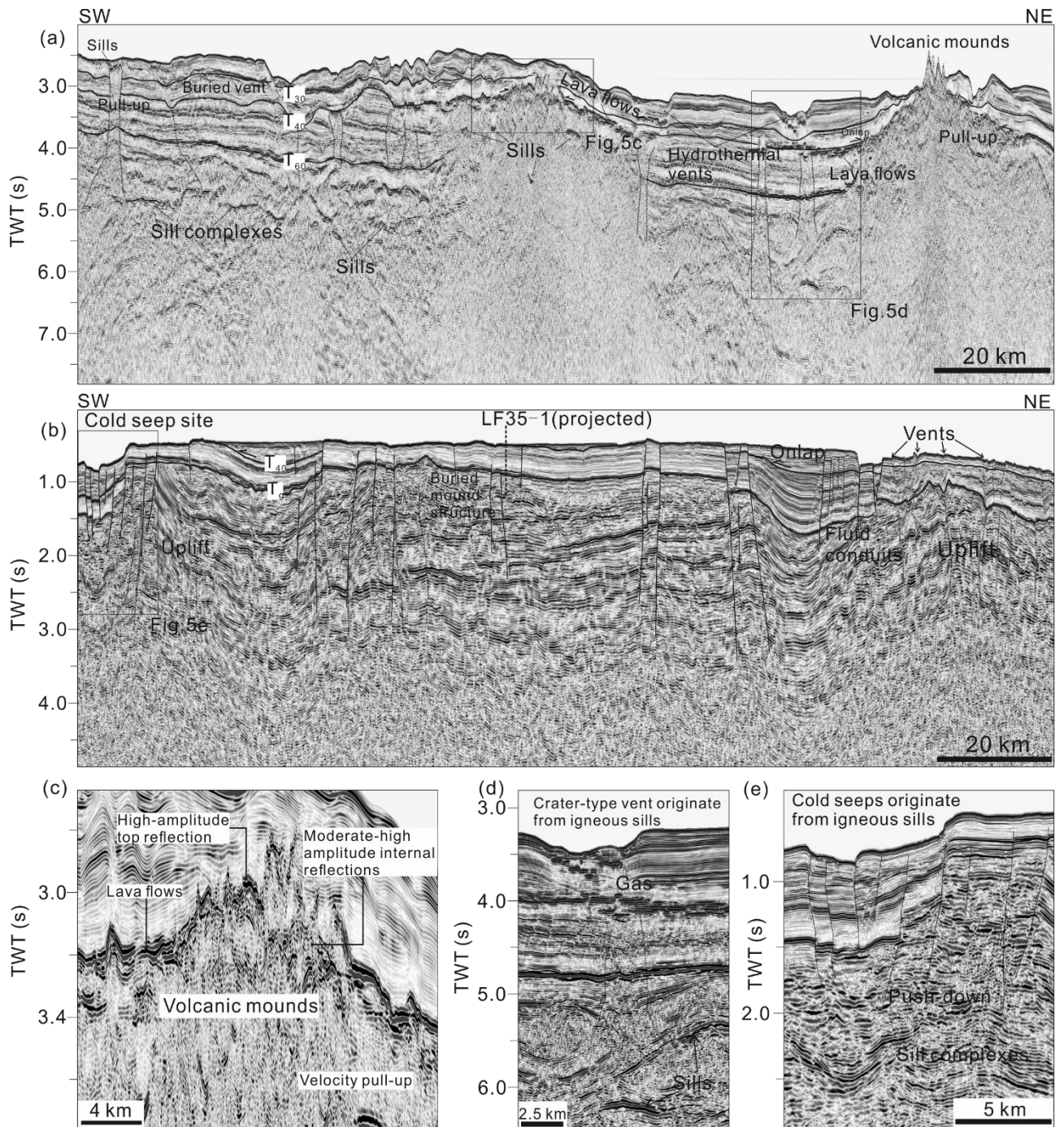


Fig. 5. (a) Interpreted multichannel seismic section highlighting the occurrence of volcanic mounds, lava flows, igneous sills and crater-type hydrothermal vents on the modern seafloor. See location in Fig. 3a. Note the onlap reflections onto volcanic mounds and lava flows providing a seismic stratigraphic indicator of magma emplacement. The vents originate above igneous sills and are linked to these latter via chimneys and pipes. (b) Interpreted multichannel seismic section (see Fig. 3a for location) highlighting structural uplift, hydrothermal venting and cold seep site at the seafloor. Note the occurrence of faulting and sediment deformation beneath the vents and cold seeps. (c), (d) and (e) Enlarged sections of (a) and (b) showing the geometry of volcanic mounds, hydrothermal vents and cold seeps linked to underlying sills.

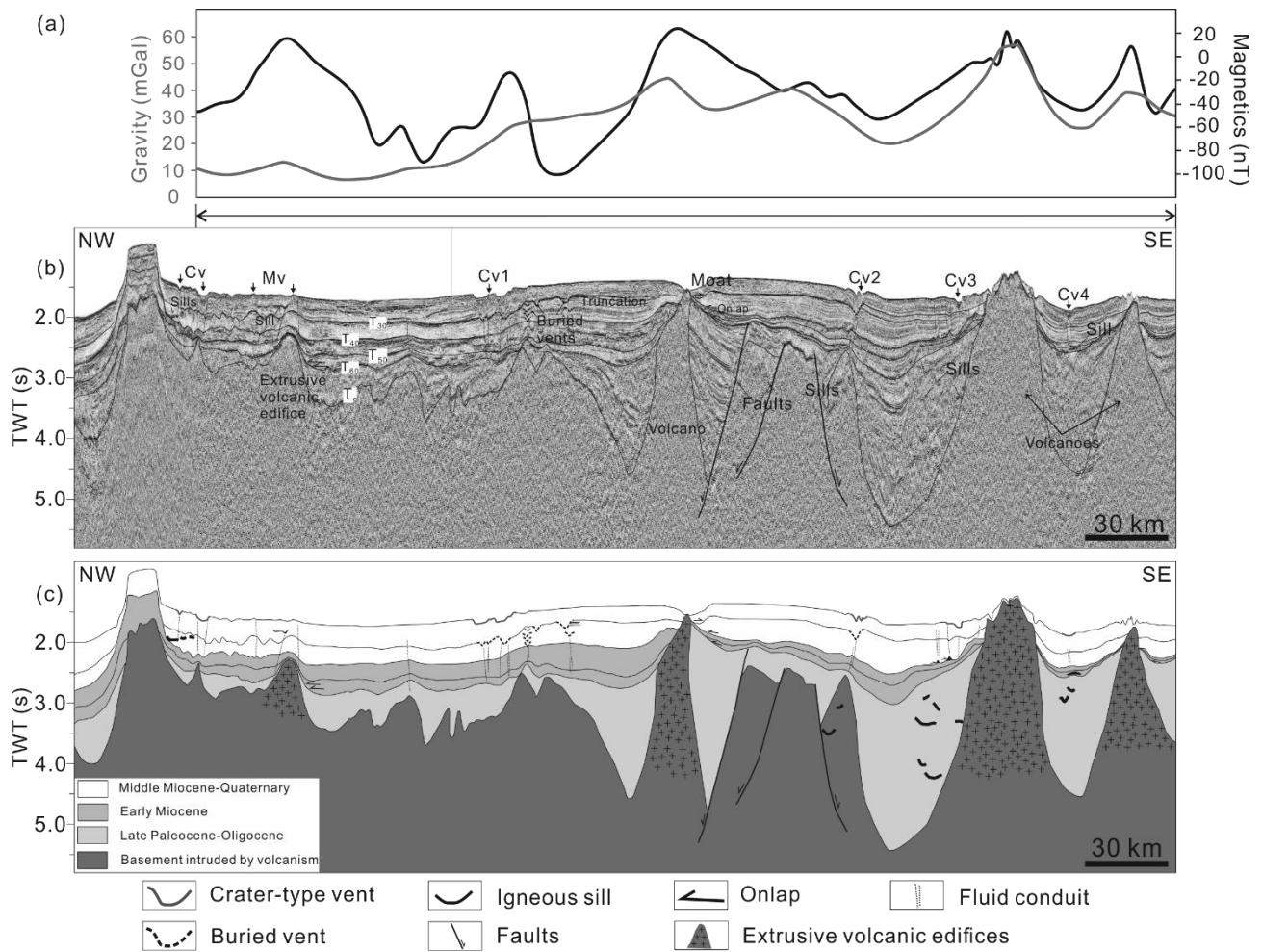


Fig. 6. (a) Gravity and magnetic anomalies acquired along the seismic profile in Fig. 6b. (b) and (c) Seismic profile and interpretation (see location in Fig. 3b) across the northwest South China Sea highlighting key seismic horizons, volcanic bodies and hydrothermal vents. Horizons T_{30} , T_{40} , T_{50} , T_{60} and T_g correspond to the base of Pliocene, Upper Miocene, Middle Miocene and Lower Miocene strata, and the top of basement, respectively. Stratigraphic correlations show extrusive edifices at three distinct stratigraphic levels. Most crater-type vents occur above Horizon T_{30} (base Pliocene) and onlap onto the post-intrusion seafloor shown in the figure.

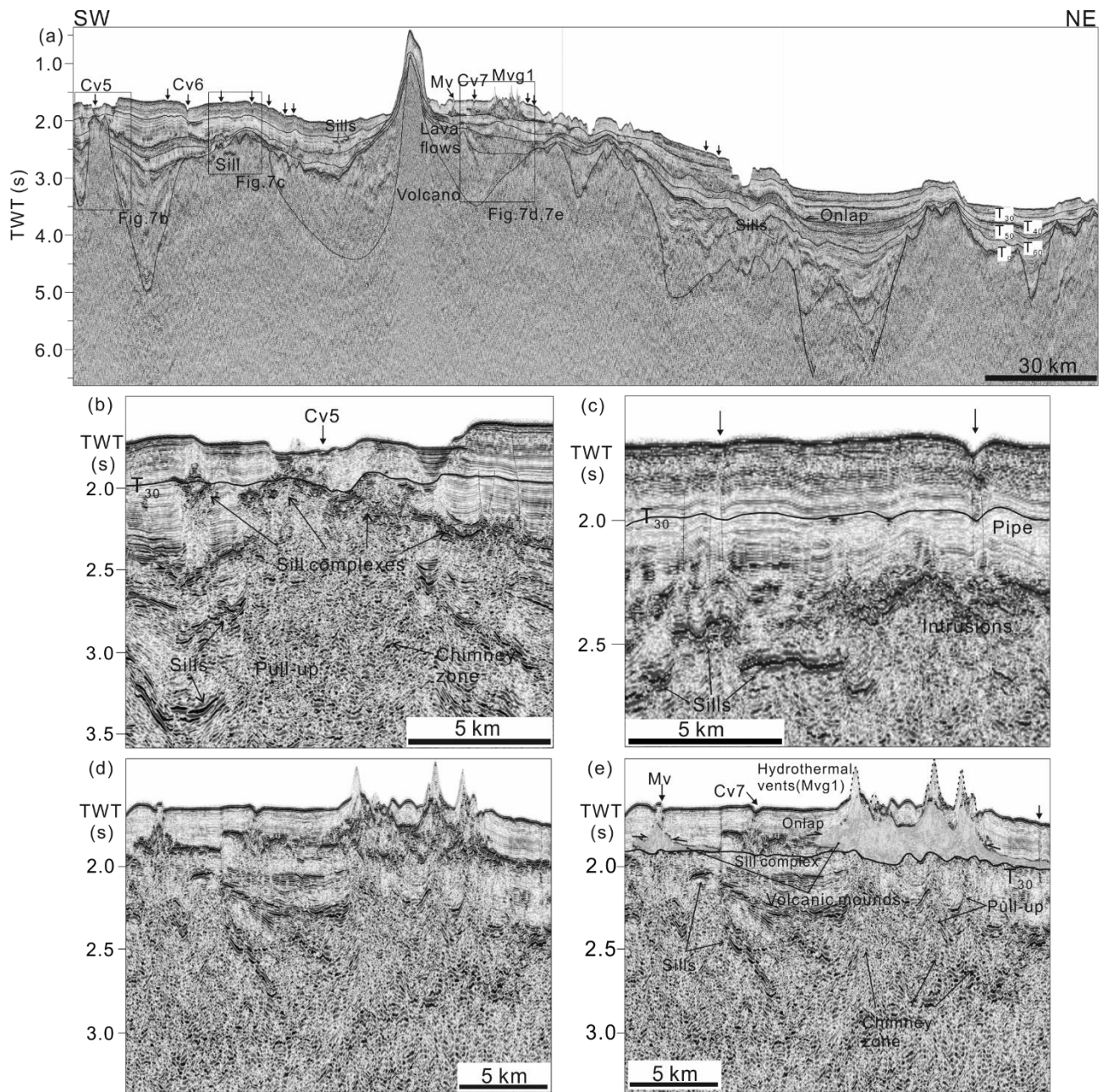


Fig. 7. (a) Regional SW–NE trending seismic cross-section (See location in Fig. 3b) revealing igneous features and hydrothermal vent complexes. Note the erosional truncation (T_{30}) of craters and onlapping reflections (T_{30}) onto the mound-type vents. (b) and (c) Enlarged section showing the geometry of mound- and crater-like vents linked to underlying sills by chimney or pipe structures. (d) and (e) Uninterpreted and interpreted seismic sections of volcanic mounds and hydrothermal vents. See Fig. 7a for location.

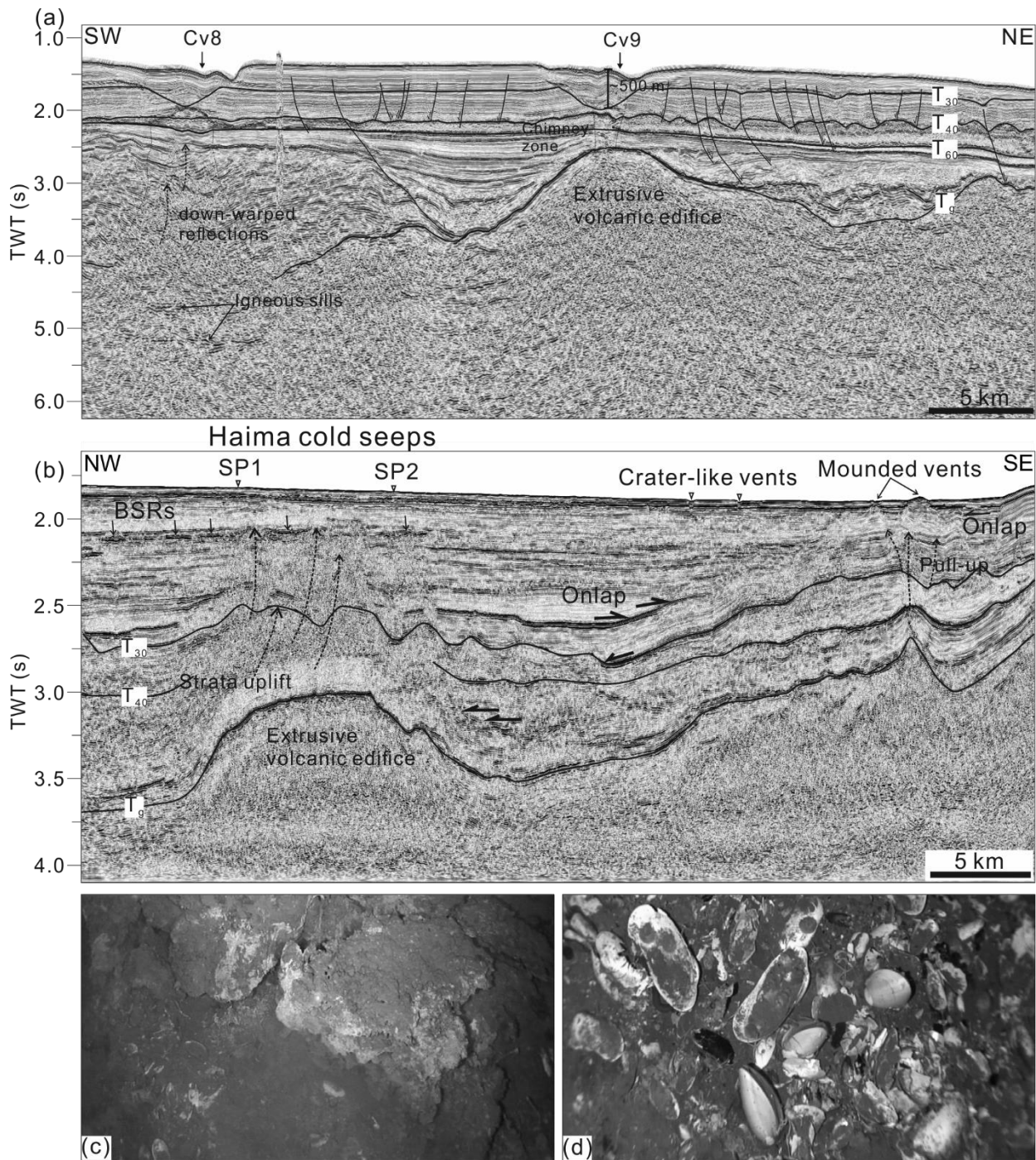


Fig.

8. (a) Interpreted seismic profile across the Zhongjiannan Basin (location shown in Fig. 3b) highlighting the presence of giant craters truncating Horizon T_{30} (5.5 Ma). Strata uplift and sediment deformation occur above the volcanic edifice, suggesting later magmatic events. (b) Regional seismic profile of the Haima seep area (Wang et al., 2018) showing local doming, BSRs and cold seeps at the seafloor. See location in Fig. 3. Sediment deformation and seismic dimming along vertical zones is clear in the seismic data. Note the different phases of onlap above Horizon T_g . (c) and (d) Photographs from the *Haima cold seeps* showing authigenic carbonate pavements (c), together with living and dead clams and related carbonate crusts (d). BSRs: bottom-simulating reflectors.

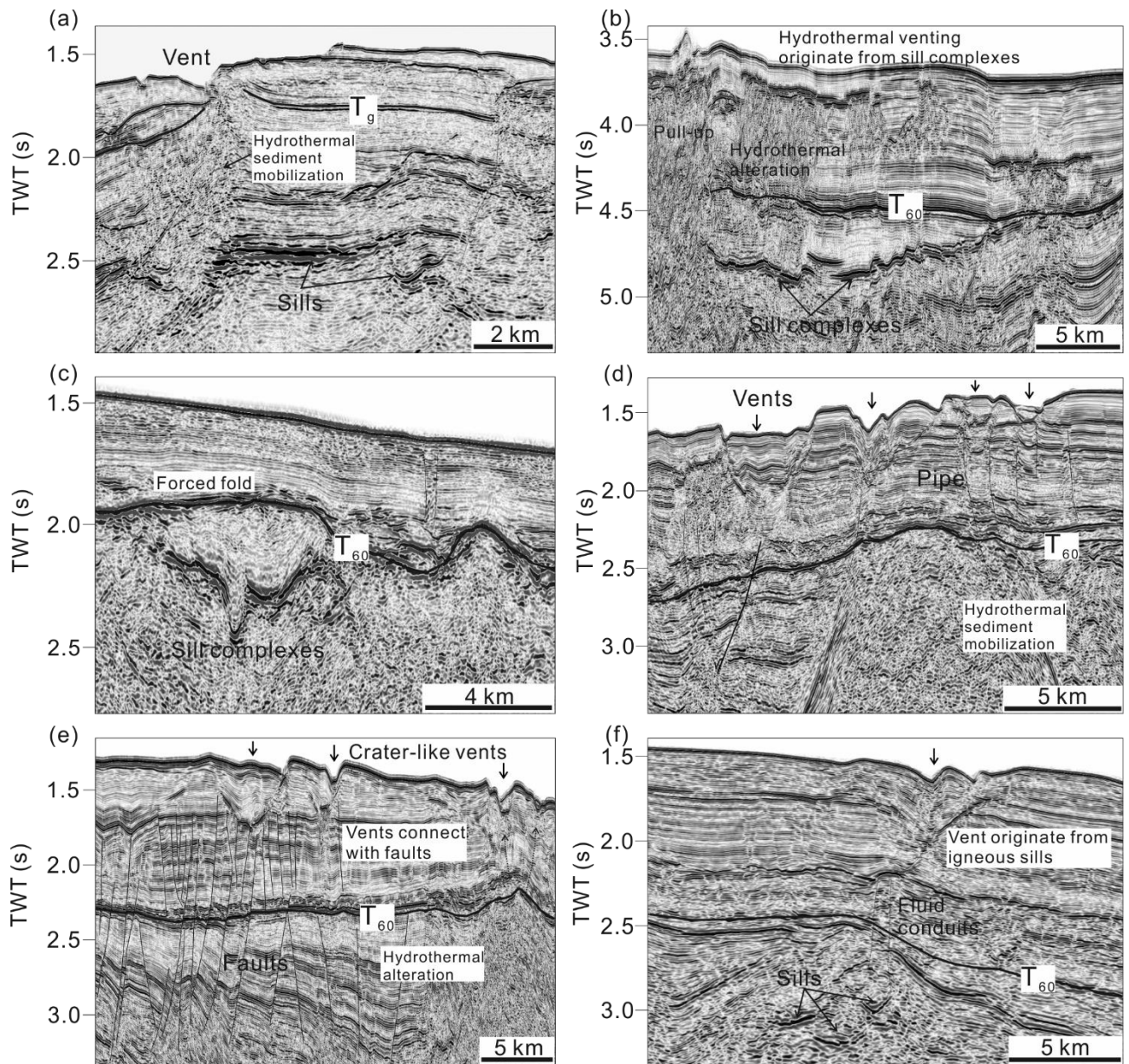


Fig. 9. Seismic examples of hydrothermal venting in the northern South China Sea. (a) Crater-type vent on the modern seafloor above buried igneous sills. (b) Hydrothermal venting connecting with an interconnected transgressive sill complex. (c) Forced-fold structure observed above a saucer-shaped sill. (d) Hydrothermal vents emanating from an underlying volcanic edifice. (e) Crater-type hydrothermal vents above faults. (f) Crater-type vent sourced from igneous sills within syn-rift strata.

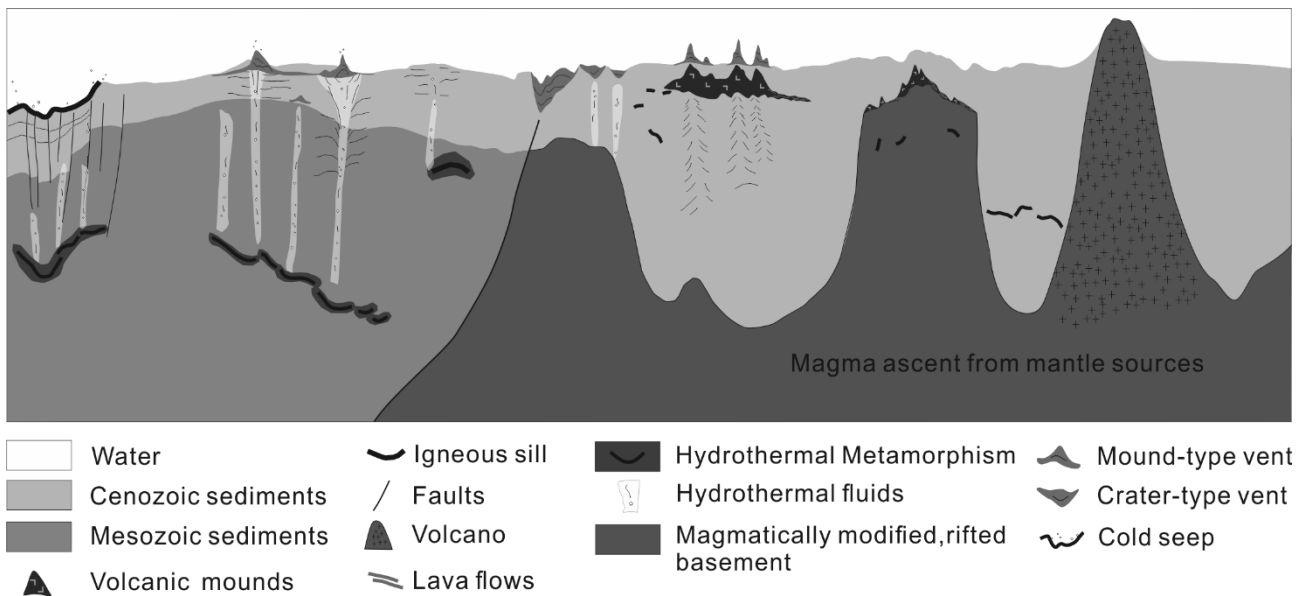


Fig. 10. Schematic diagram illustrating the main magmatic and hydrothermal processes identified in the study area.